

Leibniz-Institut für Festkörper- und Werkstoffforschung Dresden
Institut für Theoretische Festkörperphysik

Calculation of the Epitaxial Bain Path of Palladium

Diplomarbeit
zur Erlangung des akademischen Grades
Diplom-Physiker

vorgelegt von

Stephan Schönecker
geboren am 25.04.1979 in Großröhrsdorf

Institut für Theoretische Physik
Fachrichtung Physik
Fakultät für Mathematik und Naturwissenschaften
der Technischen Universität Dresden
2007

1. Gutachter: Prof. Dr. Helmut Eschrig
2. Gutachter: Prof. Dr. Peter Entel

Eingereicht am 08. August 2007

Kurzfassung

Mit Hilfe der Dichtefunktionaltheorie in der lokalen Dichtenäherung wurden Gesamtenergierechnungen für tetragonal verzerrte Gitterstrukturen von Palladium durchgeführt. Derartig verzerrte Strukturen resultieren aus heteroepitaktischem Wachstum dünner Filme auf kubische Substrate in (001) Orientierung auf Grund der vorherrschenden Gitterfehlانpassung. Ein Bestandteil dieser Arbeit war die Berechnung des sogenannten epitaktischen Bain-Pfades – einem strukturellen Übergang zwischen dem kubisch-flächenzentrierten (fcc) und dem kubisch-raumzentrierten (bcc) Kristallgitter. Die sich nicht im Grundzustand befindliche kubisch-raumzentrierte Struktur wurde in einem spannungsfreien Zustand gefunden. Entlang des Überganges von fcc zu bcc verändert sich die Anordnung der Atome in der Elementarzelle und damit konsequenterweise auch die Bandstruktur. Dies könnte zu einer ferromagnetischen Instabilität von Palladium führen. Dies beurteilten wir mittels des Stoner-Kriteriums. Anhand der Ergebnisse unserer Rechnungen zeigten wir jedoch, dass die Zustandsdichte an der Fermi-Kante für alle betrachteten Gittergeometrien jenseits des Grundzustandes rasch abfällt. Zusätzlich berechneten wir die planare Spannung und das Volumen pro Atom entlang des epitaktischen Bain-Pfades.

Abstract

We performed total energy calculations on strained tetragonal states of bulk fcc palladium by means of density functional theory using the local density approximation. Coherent epitaxial growth of thin films on cubic (001) substrates results in such strained structures due to heteroepitaxy with mismatch. We obtained what is called the epitaxial Bain path of palladium, a structural transition between the fcc and the bcc structure. We found the non-equilibrium bcc structure in a local stress-free state. Due to the change in atomic arrangement and consequently the band structure along the epitaxial Bain path, palladium might exhibit a ferromagnetic instability, which we studied by means of the Stoner criterion. However, our calculations showed that the density of states significantly decreases for any considered states compared to the one of the ground state. We computed the planar stress and the volume per atom along the epitaxial Bain path.

Table of Contents

1	Introduction and Motivation	1
2	Theory	3
2.1	Basic Density Functional Theory	3
2.2	Epitaxial Bain Path for Centred Cubic Lattices	8
2.3	Epitaxial Thin Films	14
2.4	Stoner Criterion	15
3	Computation	17
3.1	Description of the Calculation Process	17
3.2	FPLO Settings	18
3.3	Fitting Methodology and Error Estimation	22
3.3.1	Least Squares Fit for Energies	23
3.3.2	Linear Regression for In-plane Stress	26
3.3.3	Root Finding	28
3.4	States With Cubic Symmetry	29
3.4.1	Fcc Bravais lattice	29
3.4.2	Bcc Bravais lattice	30
3.5	Results and Discussion	31
3.5.1	Total Energy Along Epitaxial Bain Path	32
3.5.2	Epitaxial Bain Path	32
3.5.3	Relative Volume Along Epitaxial Bain Path	32
3.5.4	Density of States Along Epitaxial Bain Path	35
3.5.5	In-plane Stress Along Epitaxial Bain Path	37
3.6	Comparison	40
4	Summary and Outlook	43

A Representation of Exchange-correlation Potential	45
B Restriction on Elastic Constants	47
C Brillouin Zone	49
Bibliography	51

Chapter 1

Introduction and Motivation

Since its discovery in the sixties [1,2] density functional theory (DFT) has been applied to a multitude of crystalline real materials in order to study their structural, electronic and magnetic properties. Consequently it has become a very important, widely used and effective tool, pushed by the rapid development of powerful computers.

This work will use density functional theory to study palladium. What makes palladium interesting to survey?

Palladium is a 4d transition metal with a ground state free atom electronic configuration $[Kr]4d^{10}5s^0$. Since there are only completely filled electronic shells palladium has zero orbital, spin and total angular momentum, hence no (electronic) magnetic moment. Bulk palladium crystallises in the fcc structure and is, although isoelectronic to the ferromagnetic 3d nickel, not magnetic. But already a small amount of impurities of iron lead to ferromagnetic behaviour [3]. The electronic structure of bulk palladium has been studied in detail and from band calculations we know that the density of states shows a large peak located just below the Fermi energy [4,5]. The large density of states at the Fermi energy explains why palladium metal exhibits a large Pauli paramagnetic susceptibility [6,7]. An analysis based on the Stoner theory found that the Stoner criterion for ferromagnetism is nearly fulfilled [6,8].

Theoretical studies [5,9,10] for transition metals showed that an isotropic expansion of the lattice parameter by few percent lead to an onset of magnetic behaviour in palladium. In principle its presence or absence results from a competition between the exchange interaction among electrons acting intra-atomic and the inter-atomic motion of electrons [11]. A ferromagnetic ground state is favoured when the gain in exchange energy exceeds the cost in kinetic and Hartree energy due to band splitting. The inter-atomic motion is strongly affected by the separation of atoms, saying that at sufficiently large cell volumes (low densities), normally non-magnetic transition metals become magnetic when the volume is expanded – partial occupation of the

d-bands presumed. In the case of palladium the required lattice expansion is about 5% [5,9,10] or 10% [9], depending on the consideration of spin-orbit coupling. Experimentally, isotropically strained structures with expanded volumes are impossible to fabricate.

Advances in experimental techniques allowed to study non-equilibrium structures with expanded volumes, firstly demonstrated by means of heteroepitaxial growth [12]. Heteroepitaxial growth of metals on single-crystal substrates offers a promising way to produce single crystal films which may be pseudomorphic with the substrate, i.e. the film material adopts the same shape and size of unit mesh as the surface plane of the substrate material. Heteroepitaxy on a cubic (001) substrate results in tetragonal strained structures [13,14]. It may occur that all stresses on the strained tetragonal film vanish and that the corresponding total energy is locally minimal against small deformations (stress free ground state has lowest energy). Such a metastable state might possess different or new properties because the atomic arrangement is distinct from the ground state characteristics. The so-called epitaxial Bain path [15] locates all states that may form pseudomorphically on a substrate with a given symmetry.

The aim of this work is to calculate by means of density functional theory at first the geometry of epitaxial films of palladium metal on appropriate substrates. A comparable but less accurate calculation has been done earlier by Jona [14]. In order to analyse properties, which have not been discussed by Jona, the calculation has to be repeated. Secondly, investigate the magnetic structure of such strained films, driven by the introductory comments on the incipient magnetic behaviour of palladium.

This calculation is a model calculation for a bulk system, no surface or interface effects are taken into account. This is clearly a simplification of the ‘real problem’ related to a thin epitaxial film on some substrate material. But it is justified by the fact that bulk like properties are restored within few layers beyond the surface or interface [16].

This thesis discusses in the next chapter the basics of density functional theory, followed by an introduction to the subject of the epitaxial Bain path. Additionally a brief comment to epitaxial films and the Stoner criterion is given. In Chapter 3, we discuss in detail the computation of the epitaxial Bain path of palladium and we investigate how several physical properties change along the epitaxial Bain path, including an estimation of their precision. Finally this work is summarised and an outlook is presented in Chapter 4.

Chapter 2

Theory

This chapter is dedicated to provide necessary theoretical knowledge of density functional theory. The information given here reflect only a very short introduction into the field of density functional theory. Further we introduce in detail a special Bain transformation, discuss its properties and study briefly its experimental implementation. This chapter closes with a note on the Stoner criterion for ferromagnetism.

2.1 Basic Density Functional Theory

Density functional theory has evolved as a very powerful method for the investigation of electronic properties of many-electron systems. As DFT is the theory this work is based on, we would like to give a brief review for one of the simplest systems to which DFT has been applied, namely a system of non-relativistic electrons in a non-degenerate and spin-compensated ground state [17–21]. Atomic units (\hbar , $|e|$ and m equal 1) are used throughout.

Materials are built up of electrons and of nuclei of different elements and the basic interaction among these particles is Coulombic. Depending on the signs of the charge of two interacting particles the resulting force can be either attractive or repelling. Let us consider a non-relativistic system of interacting nuclei and electrons. The motion of the nuclei is essentially much slower compared to that of the electrons, due to the much higher masses of atomic nuclei. As a good approximation, the electrons can be considered to remain in its ground state all the time since they react immediate to a change of position of nuclei, e.g. to thermal oscillations. Thus, the positions of the nuclei $\mathbf{R} = \{\mathbf{R}_l\}$, $l = 1 \dots N_n$, enter the potential term in the Hamiltonian for the electronic subsystem only parametrically, whereat N_n represents the total number of nuclei in the system. This is called the *adiabatic approximation*.

For further discussion we only consider the subsystem of N electrons in

the adiabatic approximation, whose Hamilton operator \hat{H} is denoted as

$$\begin{aligned}\hat{H} &= -\frac{1}{2} \sum_{i=1}^N \nabla_i^2 + \frac{1}{2} \sum_{i=1}^N \sum_{\substack{i'=1 \\ i' \neq i}}^N \frac{1}{|\mathbf{r}_i - \mathbf{r}_{i'}|} - \sum_{i=1}^N \sum_{l=1}^{N_n} \frac{Z_l}{|\mathbf{r}_i - \mathbf{R}_l|} \\ &= \hat{T} + \hat{V}_{\text{ee}} + \hat{V}_{\text{ext}},\end{aligned}\tag{2.1}$$

where Z_l is the charge of the l 'th nucleus and $\mathbf{r} = \{\mathbf{r}_i\}$, $i = 1 \dots N$, are the positions of the electrons in the system. In Eq. (2.1) we have the kinetic energy term \hat{T} , the electron-electron repulsion \hat{V}_{ee} and the external potential \hat{V}_{ext} created by the nuclei.

The many-electron wave function $\Psi(x_1, \dots, x_N; \mathbf{R})$ for the electronic ground state can in principle be calculated by solving the Schrödinger equation

$$\hat{H}\Psi(x_1, \dots, x_N; \mathbf{R}) = E(\mathbf{R})\Psi(x_1, \dots, x_N; \mathbf{R}).\tag{2.2}$$

We have used the abbreviation $x_i = (\mathbf{r}_i, s_i)$ in the argument of the wave function Ψ , s_i represents the spin of the i 'th electron. E denotes the energy of the ground state. Note that the Hamiltonian in Eq. (2.1) does not contain spins, but of course one has to take into account the Pauli principle when constructing the wave function Ψ . We assume the ground state to be non-degenerate and hence not spin-polarised: in the notation we will not indicate the spins s_i any longer, keeping in mind the antisymmetry of the wave function due to the Pauli principle. In addition we will not state the parametric \mathbf{R} -dependence of the many-electron wave function Ψ and of the total energy E further.

For later purpose we write the external potential in a different form

$$\hat{V}_{\text{ext}} = \sum_{i=1}^N v(\mathbf{r}_i),\tag{2.3}$$

and denote v explicitly as a functional variable in the Schrödinger equation

$$\hat{H}[v]\Psi[v] = E[v]\Psi[v].\tag{2.4}$$

Although Eq. (2.1) already represents a simplified problem due to the adiabatic separation of nuclear and electronic degrees of freedom, it is still an eigenvalue problem for typically 10^{23} variables and by far not numerically manageable. Today, systems up to eight electrons can be calculated numerically by solving the Schrödinger equation on sparse grids. Density functional theory tackles the many-electron problem in a complementary perspective. It principally focuses on the electron density as basic variable. Hohenberg and Kohn [1] formulated an exact theoretical foundation for the treatment of interacting electronic systems in their non-degenerate ground state in terms of the electronic density. They showed that the ground state density

of a bound and interacting system of electrons in some external potential uniquely determines this potential, as well as other ground state properties, particularly the ground state energy E . Hohenberg and Kohn deduced a formal stationary expression for the total energy of such a system, the so called energy variational principle. Starting from this principle, Kohn and Sham [2] derived a system of self-consistent one-particle equations for the ground state – the Kohn-Sham equations.

In the following we would like to present briefly the fundamental variational formulation and the Kohn-Sham self-consistent equations. We start by introducing the new variable, the electron density of the ground state $n(\mathbf{r})$ defined by (summation over spin indices implied)

$$n(\mathbf{r}) = N \int d^3r_2 \dots \int d^3r_N |\Psi(\mathbf{r}, \mathbf{r}_2, \dots, \mathbf{r}_N)|^2, \quad (2.5)$$

with Ψ being normalised $\langle \Psi | \Psi \rangle = 1$ and

$$\int d^3r n(\mathbf{r}) = N. \quad (2.6)$$

Following the theorem of Hohenberg and Kohn we know that the external potential v is a unique functional of the ground state density n . We can substitute the functional dependence on the external potential v for a dependence on $v[n]$.

Equivalently to solve the Schrödinger equation (2.4) is the wave function variational principle, which gives us the ground state energy E by minimising $\langle \tilde{\Psi} | \hat{H} | \tilde{\Psi} \rangle$ over all normalised, antisymmetric trial wave functions $\tilde{\Psi}$ for the given number of electrons N

$$E[v] = \min_{\tilde{\Psi}} \langle \tilde{\Psi} | \hat{H} | \tilde{\Psi} \rangle. \quad (2.7)$$

Hohenberg and Kohn formulated the minimal principle in terms of trial densities rather than trial wave functions. Instead of presenting this idea we want to follow another approach by Levy [22] and Lieb [23] called the *constrained search method*. The minimisation of Eq. (2.7) is carried out in two steps. First one fixes a trial density $\tilde{n}(\mathbf{r})$ and minimises over the class of wave functions $\tilde{\Psi}^\alpha$ which yield that trial density ($\tilde{n}(\mathbf{r}) = N \int d^3r_2 \dots \int d^3r_N |\tilde{\Psi}^\alpha|^2$),

$$\begin{aligned} E[\tilde{n}(\mathbf{r}), v] &= \min_{\alpha} \langle \tilde{\Psi}^\alpha | \hat{H} | \tilde{\Psi}^\alpha \rangle \\ &= F[\tilde{n}(\mathbf{r})] + \int d^3r \tilde{n}(\mathbf{r}) v(\mathbf{r}), \end{aligned} \quad (2.8)$$

where we have defined the Hohenberg-Kohn functional F

$$F[\tilde{n}(\mathbf{r})] = \min_{\alpha} \langle \tilde{\Psi}^\alpha | \hat{T} + \hat{V}_{\text{ee}} | \tilde{\Psi}^\alpha \rangle. \quad (2.9)$$

The latter functional requires no explicit knowledge of v and is an universal functional of the trial density $\tilde{n}(\mathbf{r})$. In the second step we minimise over all N -electron densities $\tilde{n}(\mathbf{r})$

$$\begin{aligned} E[v] &= \min_{\tilde{n}} E[\tilde{n}, v] \\ &= \min_{\tilde{n}} \left\{ F[\tilde{n}(\mathbf{r})] + \int d^3r \tilde{n}(\mathbf{r}) v(\mathbf{r}) \right\}. \end{aligned} \quad (2.10)$$

During the minimisation the external potential v is held fixed and the minimising density is the ground state density $n(\mathbf{r})$.

So far we formulated the problem we started off with entirely in terms of densities \tilde{n} , but we are left with an explicitly unknown but well-defined functional $F[\tilde{n}]$ of the kinetic energy \hat{T} and interaction energy \hat{V}_{ee} , associated with \tilde{n} . The trick of Kohn and Sham was to write the functional $F[\tilde{n}(\mathbf{r})]$ in the form

$$F[\tilde{n}(\mathbf{r})] = T_0[\tilde{n}(\mathbf{r})] + \frac{1}{2} \int d^3r d^3r' \frac{\tilde{n}(\mathbf{r})\tilde{n}(\mathbf{r}')}{|\mathbf{r} - \mathbf{r}'|} + E_{xc}[\tilde{n}(\mathbf{r})], \quad (2.11)$$

with the quantity $T_0[\tilde{n}(\mathbf{r})]$ as the kinetic energy functional of a non-interacting N -particle model system with the same density as the interacting system. $E_{xc}[\tilde{n}(\mathbf{r})]$ is the so called exchange-correlation energy functional, defined by Eq. (2.11). The second term on the right hand side of Eq. (2.11) represents the classical Hartree electrostatic self-repulsion of the electron density. The functional T_0 is not explicitly known, but its existence is guaranteed by the theorem of Hohenberg and Kohn. It is given by

$$T_0[\tilde{n}] = E_{\text{non}}[v_{\text{non}}[\tilde{n}]] - \int d^3r v_{\text{non}}[\tilde{n}]\tilde{n}. \quad (2.12)$$

The subscript ‘non’ denotes the non-interacting model system. The functional $F[\tilde{n}(\mathbf{r})]$, as given in the Eq. (2.11), now enters the *Hohenberg-Kohn variation principle* (2.10). The corresponding Euler-Lagrange equations with the subsidiary condition of fixed particle number N have the form

$$\begin{aligned} \delta E[\tilde{n}(\mathbf{r}), v] &= \int \delta \tilde{n}(\mathbf{r}) \left\{ v_{\text{eff}}(\mathbf{r}) \right. \\ &\quad \left. + \frac{\delta}{\delta \tilde{n}(\mathbf{r})} T_0[\tilde{n}(\mathbf{r})] \Big|_{\tilde{n}(\mathbf{r})=n(\mathbf{r})} - \epsilon \right\} d^3r = 0, \end{aligned} \quad (2.13)$$

where we defined the effective potential v_{eff}

$$v_{\text{eff}}(\mathbf{r}) = v(\mathbf{r}) + \int d^3r' \frac{n(\mathbf{r}')}{|\mathbf{r} - \mathbf{r}'|} + v_{xc}(\mathbf{r}) \quad (2.14)$$

and the local exchange-correlation potential v_{xc}

$$v_{\text{xc}}(\mathbf{r}) = \left. \frac{\delta}{\delta \tilde{n}(\mathbf{r})} E_{\text{xc}}[\tilde{n}(\mathbf{r})] \right|_{\tilde{n}(\mathbf{r})=n(\mathbf{r})}, \quad (2.15)$$

which depends on the entire density distribution. Here ϵ is a Lagrange multiplier ensuring particle number conservation. The minimising density $n(\mathbf{r})$ is then given by solving self-consistently the single-particle equations

$$\left(-\frac{1}{2} \nabla^2 + v_{\text{eff}} - \epsilon_j \right) \phi_j(\mathbf{r}) = 0, \quad (2.16)$$

and

$$n(\mathbf{r}) = \sum_{j=1}^N |\phi_j(\mathbf{r})|^2, \quad (2.17)$$

where the sum is carried out over the N lowest occupied eigenstates ϕ_j , the *Kohn-Sham orbitals*. The eigenvalues ϵ_j ($j = 1, \dots, N$) are occupied energy levels. Equations (2.16) and (2.17) together with the definition of v_{eff} in Eq. (2.14) are the so called *Kohn-Sham self-consistent equations*, which have to be solved iteratively. The total ground state energy of the system is given by

$$\begin{aligned} E[v] = & \sum_j \epsilon_j + E_{\text{xc}}[n(\mathbf{r})] - \int d^3r n(\mathbf{r}) v_{\text{xc}}(\mathbf{r}) \\ & - \frac{1}{2} \int d^3r d^3r' \frac{n(\mathbf{r})n(\mathbf{r}')}{|\mathbf{r} - \mathbf{r}'|}. \end{aligned} \quad (2.18)$$

Kohn and Sham's idea to introduce the non-interacting reference system made it possible to take into account the most important part of the kinetic energy. The ignorance of the correlation part of the kinetic energy was displaced to the exchange-correlation E_{xc} functional, all remaining terms in the energy are known. The major disadvantage is that one has to solve a system of N coupled single particle equations instead of one equation for the density in terms of the potential. Up to now the theory is still exact, with the knowledge of the exact functional E_{xc} (or potential v_{xc}) all many-body effects are in principle included. Approximations to E_{xc} have to be found, required to be at the same time simple and accurate.

One of the most widely used approximations for the exchange-correlation functional was proposed by Kohn and Sham themselves, the *local density approximation* (LDA). The idea is to consider inhomogeneous electronic systems as locally homogeneous: within this approximation, E_{xc} takes the form

$$E_{\text{xc}} \approx E_{\text{xc}}^{\text{LDA}} = \int d^3r n(\mathbf{r}) e_{\text{xc}}(n(\mathbf{r})), \quad (2.19)$$

where e_{xc} is the exchange and correlation energy per particle of a uniform electron gas of density n . The LDA is exact in the limit of weak density variations.

In our calculation we used the parametrisation of Perdew and Wang [24] for the exchange-correlation energy per particle. In App. A we give more detailed information about the parametrisation.

2.2 Epitaxial Bain Path for Centred Cubic Lattices

Among the seven different crystal systems which correspond to the seven underlying point groups, we will consider in the following the crystal system with tetragonal symmetry [25]. Two different Bravais lattices belong to the latter crystal system, the simple tetragonal (st) Bravais lattice and the centred tetragonal (ct) Bravais lattice. The dimensions of the conventional unit cell of the ct lattice are described by two lattice parameters, say a and c , where a denotes the length of the square base and c the height of the tetragonal cell (alternative nomenclature by lattice configuration (a, c)). For certain ratios c/a the ct Bravais lattice reveals higher symmetric properties than the tetragonal class exhibits. Both the body-centred cubic (bcc) and the face-centred cubic (fcc) Bravais lattice represent special cases of the more general ct unit cell. If the width-to-height ratio of the lattice constants c/a equals 1, the ct Bravais lattice coincides with the bcc lattice. On the other hand a ct Bravais lattice with $c/a = \sqrt{2}$ fully matches the fcc lattice, shown in Fig. 2.1 schematically. In principle there is no restriction

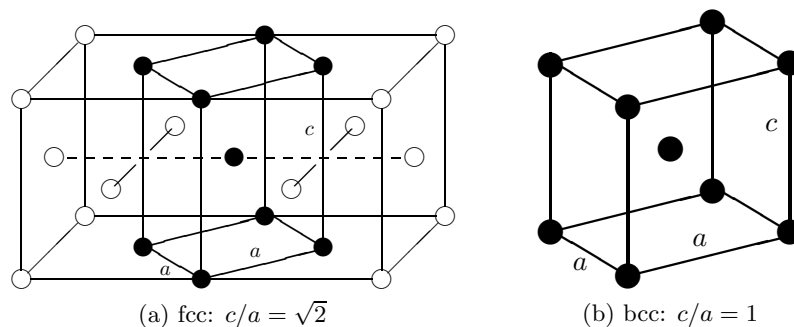


Figure 2.1: The centred tetragonal unit cell with lattice parameters a and c at special ratios c/a . Atoms belonging to the conventional unit cell are indicated by solid dots. The lattice matches both the cubic fcc and bcc Bravais lattices at width-to-height ratios given in the corresponding sub-figures.

on the choice of possible lattice configurations (whether the choice for the

lattice dimension seems physically reasonable or not). There are two parameters free to choose, each choice representing a unique configuration. The corresponding structure space (also phase space, parameter space) is two-dimensional and is referred to as the *tetragonal plane*, spanned by a' and c' (the prime symbols are used in order to distinguish the labelling of axes from an actual configuration). Each point in the tetragonal plane belongs to another lattice configuration (a, c) . Of course higher symmetric centred cubic structures can be located in the tetragonal plane, see Fig. 2.2. Due to their fixed ratio c/a they are localised along straight lines through the point of origin with slopes defined by the actual values of the ratio c/a . The fcc and bcc structures lie on lines with slopes $\sqrt{2}$ and 1, respectively.

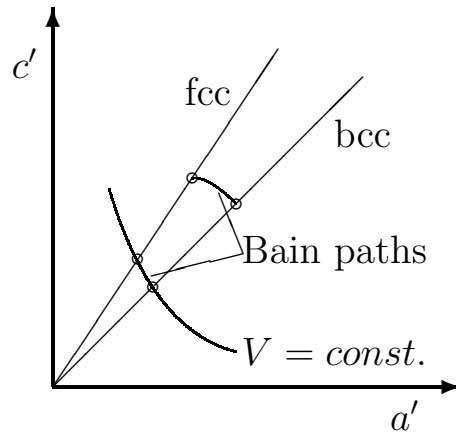


Figure 2.2: The structure space for the ct Bravais lattice is two-dimensional and spanned by a' and c' . Centred cubic structures are special cases of the ct unit cell and located on straights. A Bain transformation connects both cubic structures via tetragonal distortions of the unit cell (start and end marked by circles \circ), such as the constant volume Bain path. This path follows a hyperbola.

We now study a transformation between the body-centred cubic and the face-centred cubic structure (or vice versa). It was Bain [26] who originally described such a transformation by a continuous and coordinated shifting of one or more atoms in the unit cell in order to understand the mechanism of the transition from austenite to martensite in iron. The austenitic high-temperature phase (fcc) undergoes a first order transition to the martensitic low-temperature phase (bcc), whose structural change Bain described via tetragonal distortions by a continuous change of a single variable (the ratio c/a) with the (001) plane of both structures remaining unmodified. A transformation that connects face-centred and body-centred cubic structures via tetragonal distortions is a so-called *Bain transformation*. It is easily seen that this structural change can be traced in the tetragonal plane. Each state

along the transition corresponds to a certain point in the tetragonal plane and, if we require that the transition is continuous (no first order phase transitions), we obtain a line in the tetragonal plane, the *Bain path*. Since one allows for tetragonal distortions only, all applied distortions retain tetragonal symmetry of the unit cell. It should be noted that there exist many different Bain paths, exemplary the constant volume Bain path and the epitaxial Bain path should be mentioned. The Bain transformation along the constant volume path contains all configurations having the same, during the transition unchanged, volume per atom $V = a^2c/2$. The single independent variable is, for instance, the lattice parameter a , the second lattice constant c is fixed by the condition of constant volume. Constant volume Bain paths are hyperbolas in the tetragonal plane. The epitaxial Bain path represents another Bain transformation which is subject to different constraints and will be discussed in the following in more detail. Note that from the earlier definition as a structural transition, a Bain path is supposed to start and to end at structures of cubic symmetry. Over and above that we will use the same term if a Bain transition is extended beyond the confine of cubic structures.

The epitaxial Bain path (EBP) is a unique path through the tetragonal plane, whereat each state belonging to the transformation is characterised by the following two conditions [15]

- isotropic in-plane [(001) plane] stress

$$\sigma_1 = \sigma_2 \quad (2.20)$$

- vanishing out-of-plane ([001] direction) stress

$$\sigma_3 = 0 \quad (2.21)$$

where the σ_m , $m = 1 \dots 6$, are the components of the stress tensor (σ_m) in vector notation.¹ All other elements of σ vanish as well. While the applied in-plane stress can be tensile or compressive (or zero), vanishing out-of-plane stress requires the unit cell in the [001] direction to be relaxed in any case. Figure 2.3 sketches this in a descriptive way. As we will see later on such conditions can in principle be realised in epitaxial thin films. It is easily seen that these conditions conserve the tetragonal symmetry of the unit cell, since isotropic in-plane stresses leave the basal plane quadratic and there are no additional shears which could break tetragonal symmetry. The solution of the Kohn-Sham equations (Eq. (2.18) on Page 7) provides the total energy per atom $E(a, c)$ for the specific lattice configuration (a, c) . This will be called a state of the system. From the first derivatives of the

¹ σ_{ij} is the rank two tensor of stress. In vector notation, the ij 's are replaced by a single index: 11 \rightarrow 1; 22 \rightarrow 2; 33 \rightarrow 3; 23, 32 \rightarrow 4; 13, 31 \rightarrow 5; 12, 21 \rightarrow 6

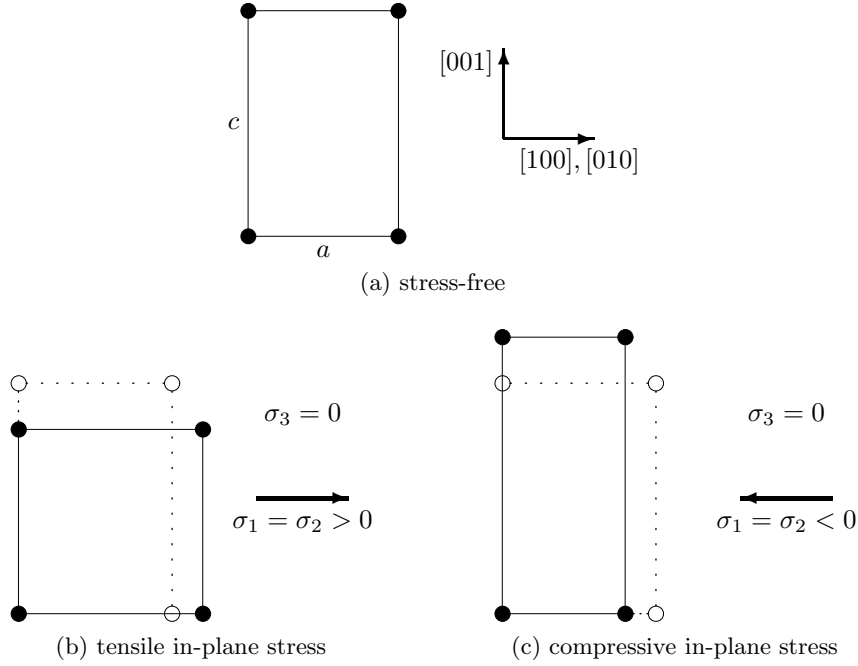


Figure 2.3: Descriptive illustration of Conditions (2.20) and (2.21). (a) shows the stress free ground state (atom positions denoted by solid dots). The sides of the crystal coincide with the axis of reference. In (b) the crystal suffers a planar isotropic tensile stress in the (001) plane. No force is applied from the [001] direction. Consequently the side c will relax to lower the energy of the strained crystal. As a result the in-plane lattice sides are expanded, the out-of-plane lattice parameter is reduced (in (b) and (c): atom positions without applied stress denoted by open dots, with applied stress by solid dots). (c) refers to the opposite case of isotropic compressive in-plane stress. The in-plane lattice constant shrinks while the out-of-plane lattice parameter expands.

total energy per atom with respect to lattice parameters one can obtain the in-plane and out-of-plane stresses

$$\sigma_1(a, c) = \sigma_2(a, c) = \frac{1}{ca} \left. \frac{\partial E(a', c')}{\partial a'} \right|_{a, c} \quad (2.22)$$

$$\sigma_3(a, c) = \frac{2}{a^2} \left. \frac{\partial E(a', c')}{\partial c'} \right|_{a, c}. \quad (2.23)$$

For each lattice constant a , Condition (2.21) with Eq. (2.23) gives the c value at which the first partial derivative of the total energy with respect to c' vanishes. This particular value will be designated $c_{\text{EBP}}(a)$ and we find the stress-free state at c_{EBP} , $\sigma_3(c_{\text{EBP}}) = 0$. The corresponding value for the energy will be denoted by $E_{\text{EBP}} = E(c_{\text{EBP}})$. In principle, Eq. (2.21) is

fulfilled for a maximum, a minimum or an horizontal inflection point in total energy. We will assume a ‘normal’ bonding energy dependence applicable for layers $E(a = \text{const}, c)$, i.e. at small values of c the layers repel each other (energy increases), and at large distances the layers pass into the unbound state. In between there is a state, which is a minimum in total energy for the given value of a .

The lattice parameter c_{EBP} will be different for distinct a values, hence a function of a , as the total energy at c_{EBP} is as well. The epitaxial Bain path is obtained by solving Eq. (2.21) for each a . Thus, one obtains two dependencies on the single variable a , the actual Bain path in the tetragonal plane $c_{\text{EBP}}(a)$ and the total energy, $E_{\text{EBP}}(a) = E(a, c_{\text{EBP}}(a))$.

The epitaxial Bain path locates one tetragonal stable and further tetragonal meta-stable phases of a given crystal. The tetragonal stable phase is the ground state of the underlying crystal, which is in many cases fcc or bcc. Meta-stable phases are non-equilibrium states with higher energy than the ground state.

Cubic structures exhibit a vanishing first derivative of the total energy along the epitaxial Bain path $E_{\text{EBP}}(a)$ with respect to the in-plane lattice parameter a . This can be shown by a symmetry argument [15]. At an extremum or horizontal inflection point of $E_{\text{EBP}}(a)$ both the first derivatives of $E(a, c)$ with respect to a and with respect to c vanish, the latter of course by construction of the EBP. Thus, no stresses at all are present at extrema or horizontal inflection points of the epitaxial Bain path

$$\sigma_1 = \sigma_2 = \sigma_3 = 0. \quad (2.24)$$

In the following we state the conditions for (meta-) stability of tetragonal crystalline phases. These conditions arise from the demand of positive definite strain energy (that is the work necessary to produce a strain). Otherwise the crystal would be unstable. In terms of the elastic constants for the considered tetragonal class c_{ij} , $i, j = 1 \dots 6$, the conditions are

$$c_{11} > |c_{12}| \quad (2.25)$$

$$(c_{11} + c_{12}) c_{33} > 2c_{13}^2 \quad (2.26)$$

$$c_{44} > 0 \quad (2.27)$$

$$c_{66} > 0. \quad (2.28)$$

These conditions are deduced in App. B. In order to verify the stability conditions the individual elastic constants have to be calculated, e.g. from derivatives of the total energy with respect to deformations. Such deformations can conserve or break tetragonal symmetry. Let a_1 , a_2 and c be the sides of a triclinic crystal, θ_{12} , θ_{23} and θ_{31} the angles between adjacent sides. For a tetragonal crystal follows $a_1 = a_2 = a$ and $\theta_{12} = \theta_{23} = \theta_{31} = \frac{\pi}{2}$ (see Fig. 2.4 for a sketch). The stability conditions are presumably calculated

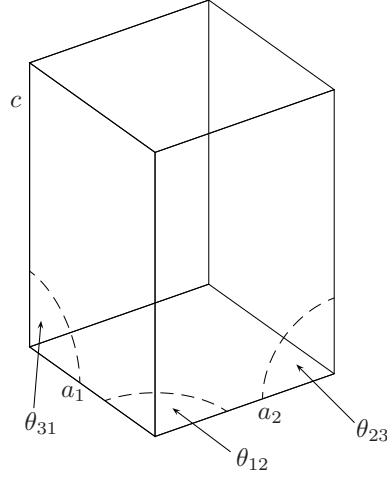


Figure 2.4: The figure sketches a triclinic crystal with side lengths a_1 , a_2 and c . In the tetragonal case the basal plane is quadratic, $a_1 = a_2$. Angles between adjacent sides are marked in the figure, being rectangular in the tetragonal case.

at minima in energy of the epitaxial Bain path, but hold general meaning. Then [27]

$$c_{11} = \frac{2}{c} \frac{\partial^2 E(a'_1, a'_2, c')}{\partial a_1'^2} \Big|_{a_1, a_2, c} \quad (2.29)$$

$$c_{11} + c_{12} = \frac{1}{c} \frac{\partial^2 E(a', c')}{\partial a'^2} \Big|_{a, c} \quad (2.30)$$

$$c_{33} = \frac{2c}{a_1'^2} \frac{\partial^2 E(a', c')}{\partial c'^2} \Big|_{a, c} \quad (2.31)$$

$$c_{11} + c_{12} - \frac{2c_{13}^2}{c_{33}} = \frac{1}{c} \frac{\partial^2 E_{\text{EBP}}(a')}{\partial a'^2} \Big|_a \quad (2.32)$$

$$c_{44} = \frac{2}{ca^2} \frac{\partial^2 E(a', c', \theta_{23})}{\partial \theta_{23}^2} \Big|_{a, c, \frac{\pi}{2}} \quad (2.33)$$

$$c_{66} = \frac{2}{ca^2} \frac{\partial^2 E(a', c', \theta_{12})}{\partial \theta_{12}^2} \Big|_{a, c, \frac{\pi}{2}} \quad (2.34)$$

In Eq. (2.29) only a'_1 is varied and a'_2 is held fixed, whereas in Eq. (2.30) a'_1 and a'_2 are varied simultaneously. The energy along the epitaxial Bain path, $E_{\text{EBP}}(a)$, enters Eq. (2.32) and must be calculated in advance of course. The second derivative of the total energy with respect to a' in Eq. (2.32) is the curvature along the EBP. At positive curvature Condition (2.26) is fulfilled, which is the case at minima of the EBP. Hence at maxima of the

EBP Eq. (2.26) is violated and the state is inherently unstable. The shear deformations which lead to the determination of the elastic constants c_{44} and c_{66} change the angles θ_{23} and θ_{12} between the sides a_2 and c and a_1 and a_2 , respectively. The deformations in Eq. (2.33) and in Eq. (2.34) lead to a monoclinic cell.

2.3 Epitaxial Thin Films

The word epitaxy deduces from two words of Greek origin, *epi* and *taxis*, meaning ‘located on’ and ‘arrangement’, respectively. Following [28], an epitaxial growth refers to the situation when atoms in the single crystal film at the interface occupy natural lattice sites of the single crystal substrate. Epitaxy means a continuation of the arrangement of crystallographic atomic positions in the substrate into the overlayer. Substrate and film material need not necessarily be of the same crystal class or material. If both materials are not of the same kind one commonly refers to heteroepitaxy, otherwise homoepitaxy. The substrate material provides a template for aligning the first layer of atoms of the film. In layer-by-layer film growth (Frank-van der Merwe growth) each grown top-layer serves the same function for the next layer. Alternative growth modes are island growth (Volmer-Weber growth) and a combination of layer-by-layer and island growth (Stranski-Krastanov growth). In general the stress-free in-plane lattice constants (parallel to the interface) of the substrate and the film need not to be identical. This is normally the case for heteroepitaxy due to the lattice mismatch. During the epitaxial growing the atoms of the film material position themselves at lattice sites aligned with those of the substrate to locally minimise the free energy. The film grows coherently (see Fig. 2.5 for an illustration). In trying to align with the substrate the film material along the interface takes strain. The mismatch strain ϵ_m is given by

$$\epsilon_m = \frac{a_s - a_f}{a_f} \quad (2.35)$$

with a_f and a_s denoting the stress-free lattice dimensions in the direction parallel to the interface for the film and the substrate, respectively. Although the coherent growth process is accompanied by elastic strain energy in the film, the energy gain associated with the chemical bonding in the process exceeds the cost of adding material with strain, at least for thin films. Once being aligned to the atomic positions of the substrate material the in-plane lattice dimensions of the thin film are fixed to those of the substrate. In the direction perpendicular to the interface a partial decrease of stored strain energy is possible by relaxation of the lattice parameter perpendicular to the interface. A thin film is considered to be relaxed in the direction perpendicular to the interface if the out-of-plane stress vanishes (see Fig. 2.3 on

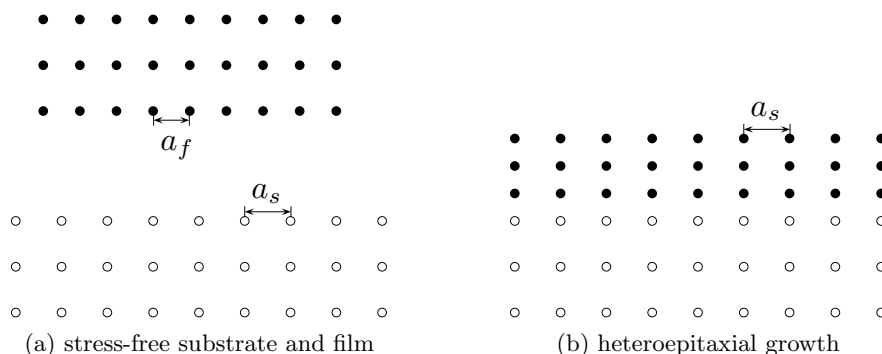


Figure 2.5: Illustration of heteroepitaxial film growth with lattice mismatch. (a) The substrate (atom positions denoted by open dots) with in-plane lattice constant a_s is assumed to be laterally further extended compared to any thickness. The film thickness with lattice dimension parallel to the surface a_f (atom positions denoted by solid dots) is presumed to be much smaller than the thickness of the substrate. (b) The film grew coherently on the substrate. Its growing is accommodated by elastic strain.

Page 11 and explanation given in the text). Accordingly, epitaxial growth on cubic (001) substrates typically results in strained tetragonal structures. As the thickness of the coherent film increases the stored strain energy per unit area in the film increases linearly with the thickness of the film (assuming uniform elastic strain over the growth area and constant volume strain energy beyond few atomic layers). Consequently the accumulated strain energy gives rise to a number of possible physical mechanisms for relaxation of strain. Such are for example misfit dislocations and change in surface morphology.

2.4 Stoner Criterion

An atom with a partially filled electron shell is magnetic and obeys Hund's rules, while ordered magnetism in solid states at room temperature is rather exceptional. Among the elemental metals, the transition metals iron, cobalt and nickel are ferromagnetic; chromium and manganese are anti-ferromagnetic. The ground state ($T = 0$ K) properties of many magnets can be understood in the itinerant electron picture [29]. Stoner [30] firstly proposed a band model for the ground state which supplied a criterion for a ferromagnetic instability. A Stoner-like band model can be derived from density functional theory formalism including spin polarisation [8,29], which is an extension of the density functional theory described in Sec. 2.1. Instead of the (spin-independent) electron density $n(\mathbf{r})$ one now deals with spin-dependent electron densities, $n^+(\mathbf{r})$ and $n^-(\mathbf{r})$, where $+$ and $-$ signs

indicate different (opposite) spin directions. Interactions with an external magnetic field \mathbf{H} can be addressed. Analogously to the spin-independent case the Hohenberg-Kohn variational principle and the Kohn-Sham equations are formulated. The local spin density approximation (LSDA) approximates the exchange-correlation energy for the inhomogeneous electron gas by that of a homogeneous electron gas with constant electron density and constant magnetisation.

The Stoner model provides a sufficient criterion for an instability. A transition to a ferromagnetic ground state is favoured when the energy gain in exchange energy (when spins arrange parallel) exceeds the cost in kinetic and Hartree energy. This is expressed by means of the *Stoner criterion*. For zero external magnetic field it is given by

$$I \cdot D(E_F) > 1, \tag{2.36}$$

where I is the Stoner parameter and D the density of states (DOS) at the Fermi energy E_F in the non-spin-polarised case. Thus, ferromagnetism is in possible in cases of a large Stoner parameter and, more important, a high density of states at the Fermi level [29].

Chapter 3

Computation

Within this chapter we describe systematically the calculation of the epitaxial Bain path of palladium. Since we do calculations with a numerical band-structure scheme it is necessary to have a closer look on required settings and how they should be specified. Further we give a summary of the inevitable fitting and data interpretation. Results are presented for bulk palladium metal and compared with literature. We investigate the possible occurrence of ferromagnetism in palladium for states along the epitaxial Bain path by means of the Stoner criterion.

3.1 Description of the Calculation Process

In Sec. (2.2) we demanded two conditions that all states constituting the epitaxial Bain path must fulfil, see Eqs. (2.20) and (2.21). We concluded that in order to obtain the EBP it is necessary to know the states of vanishing out-of-plane stress ($\sigma_3(c_{\text{EBP}}) = 0$) for each in-plane lattice parameter a . Thus we obtain c_{EBP} as a function of a , $c_{\text{EBP}}(a)$. States of vanishing out-of-plane stress can be found by total energy calculations and ascertaining the minimum in energy according to Eq. (2.23). Additionally we get the total energy along the epitaxial Bain path, $E_{\text{EBP}}(a)$, on which we can locate stable and meta-stable tetragonal states. The recipe for the calculation of the epitaxial Bain path comprises essentially the following steps

1. Select an area in the tetragonal plane (two intervals for a and c) for configurations for which calculations are supposed to be done. Choose the density of the grid. It might be necessary to adjust the intervals or change the density of the grid at a later stage.
2. Calculate the total energy for the series of c values with some initial a fixed. Perform a fit to the evaluated energies and determine the coordinates of the minimum c_{EBP} and E_{EBP} .

3. Repeat Step 2 for all selected a values and plot $c_{\text{EBP}}(a)$ and $E_{\text{EBP}}(a)$ or related properties along the epitaxial Bain path.

Concerning Step 1 we have chosen the initial intervals and grids of the lattice parameters a and c as

- $2.50 \text{ \AA} \leq a \leq 3.50 \text{ \AA}$ with step size 0.02 \AA (equidistant)
- $2.00 \text{ \AA} \leq c \leq 5.00 \text{ \AA}$ with step size 0.15 \AA (equidistant),

according to the work by Jona and Marcus [14]. The interval for a did not need to be adjusted during the calculation process, nevertheless we have chosen some additional intermediate values where appropriate.

The experimental lattice constant for fcc palladium is [31]

$$c_{\text{exp}}^{\text{fcc}} = 3.890 \text{ \AA}. \quad (\text{experimental lattice constant})$$

Expressed in terms of the centred tetragonal Bravais lattice the experimental lattice constant amounts to

$$c_{\text{exp}}^{\text{ct}} = c_{\text{exp}}^{\text{fcc}} = 3.890 \text{ \AA} \quad (\text{experimental lattice constants})$$

$$a_{\text{exp}}^{\text{ct}} = c_{\text{exp}}^{\text{ct}} / \sqrt{2} \approx 2.751 \text{ \AA} \quad (\text{using ct cell})$$

and are thus contained in the intervals stated above. The initial choice of the interval and of the grid for c provided a basis for a first guess in search of the minimum c_{EBP} for each fixed a . Since the interval for c as stated above is rather coarse and the distance between adjacent points is far, it is improper for an accurate determination of its minimum position c_{EBP} by fitting. To improve this point we performed additional calculations near by the first guess of c_{EBP} for each a . We ended up with 10 calculated total energies in an interval of 0.1 \AA around the minimum. These values entered the fit later on (more details in Sec. 3.3).

3.2 FPLO Settings

Before we can start any calculation with a numerical band-structure scheme we have to deal with a number of settings that must be chosen in advance, such as geometry, basis or the number of k -points corresponding to our problem. But only the latter needs a few more calculations to be carried out, since one would like to know the sufficient number of k -points that stabilises the total energy at a certain level. Thus, after choosing the basis and the geometry the first task is the convergence of k -point sampling, described in the next paragraph.

All calculations were done with the Full Potential Local Orbital band-structure scheme version 5 release 19 (FPLO5.00-19) [32] in scalar relativistic mode using the exchange correlation potential version of Perdew

and Wang 92 [24]. Convergence conditions are both density and energy, in detail the accuracy for the energy is 10^{-8} Hartree and for the density it is 10^{-6} unitvolume $^{-1}$. The single Wyckoff position is Pd(0,0,0). The selected space group for the calculation of the epitaxial Bain path is I4/mmm (No. 139).

The basis set was chosen to be

$$\underbrace{1s2s2p3s3p3d}_{\text{core}} :: \underbrace{(4s4p)}_{\text{semi-core}} / \underbrace{5s5p4d}_{\text{valence}} +.$$

No polarisation states were used. The division into different basis states (core, semi-core, valence and polarisation) implicates a different numerical treatment and is based on physically motivated assumptions, more precisely spacial extend and occupation of orbitals. Core and semi-core states are fully occupied, but semi-core orbitals from neighbouring sites overlap slightly one another in contrast to core states, which virtually do not overlap. Valence states do overlap significantly and are only partly occupied. Weakly occupied polarisation states eventually complete the basis set. The choice of 4s and 4p orbitals as semi-core basis states is justified by their slight overlap among nearest neighbouring (NN) sites, see Fig. 3.1. The distance among nearest neighbours in fcc palladium equals $c_{\text{exp}}^{\text{fcc}}/\sqrt{2} \approx 2.751$ Å. Our choice of the basis set is considered as appropriate for all lattice configurations used. As a precaution we checked the out-file of every calculation for potential warnings referring to the basis.

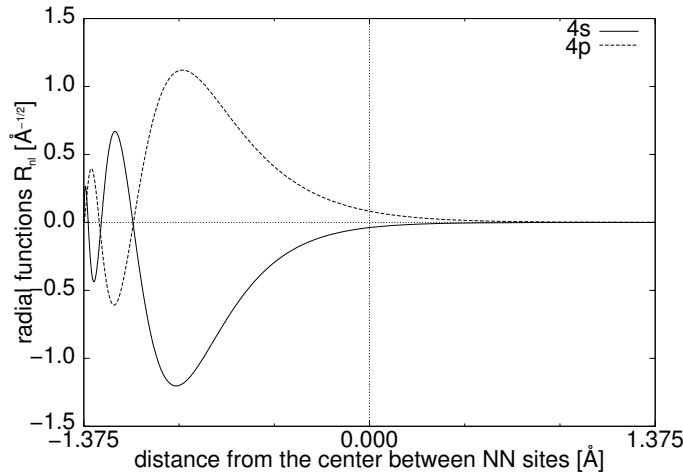


Figure 3.1: Radial functions R_{nl} for 4s and 4p orbitals of palladium of NN sites (n principal quantum number, l angular momentum quantum number). Note that the first atom is assumed to be at the half NN distance at -1.375 Å, a second be at a distance of $+1.375$ Å from the common centre. Radial functions are only plotted for the left-sided atom.

k-point sampling

This paragraph discusses the *k*-point sampling in order to get reliable information about the minimum number of *k*-points needed to ensure stability of the calculated total energy at a certain level. With the FPLO settings from the last paragraph we did a number of total energy calculations for palladium, in principle equal to Step 2 of the procedure ‘calculation of the epitaxial Bain path’ as described on Page 17. For one fixed lattice parameter *a*, total energies $E(c, k)$ were evaluated on a grid of *c* values and for different number of *k*-points. For each number of *k*-points we obtained the minimum of the fit function to the evaluated total energies, say here $c_{\min}(k)$ and the corresponding total energy $E_{\min} = E(c_{\min}, k)$. Both values depend on the number of *k*-points, since all calculated energies depend on the number of *k*-points. Thus, we studied the change of $c_{\min}(k)$ and $E_{\min}(k)$ with increasing number of *k*-points.

We have chosen for *a* the experimental lattice parameter, $a = c_{\text{exp}}^{\text{ct}}/\sqrt{2} \approx 2.75 \text{ \AA}$. The lattice parameter *c* was varied around the value found in experiment ($c_{\text{exp}}^{\text{fcc}}$), ten equidistant points for *c* were selected (distance 0.01 Å). The fit function is a fourth order polynomial. Note that ten sampling points and a fourth order polynomial are always used in this work to fit $E(c)$ curves (for more detail see Sec. 3.3).

For the number of *k*-points we chose the values 12, 20, 30, 40, 50 and 60 (in each direction in *k*-space). Beginning with 12 we increased the number stepwise and calculated the difference in energy ΔE_{\min} and lattice constant Δc_{\min} at any time with the values obtained from the calculation with next smaller *k*, i.e.

step <i>i</i>	difference in energy	difference in lattice constant
1	$E_{\min}(k = 20) - E_{\min}(k = 12)$	$c_{\min}(k = 20) - c_{\min}(k = 12)$
2	$E_{\min}(k = 30) - E_{\min}(k = 20)$	$c_{\min}(k = 30) - c_{\min}(k = 20)$
⋮	⋮	⋮
5	$E_{\min}(k = 60) - E_{\min}(k = 50)$	$c_{\min}(k = 60) - c_{\min}(k = 50)$

The evaluated differences in energy $\Delta E_{\min}(i)$ are graphically presented in Fig. 3.2. Supplementary to this figure we tabulated the evaluated numbers and give corresponding errors in Table 3.1. Concerning the errors we here anticipate on the results of Sec. 3.3. The errors listed in Table 3.1 arise from the fitting of the total energies and incorporate numerical fluctuation of the data. Its determination will be discussed in detail in Sec. 3.3.

What we find from the numbers is, that at first the error associated with the fitting in dependence on the number of *k*-points decreases with increasing number of *k*-points. This relation holds until the *k*-points equal 30. For higher *k*-values the errors remain at the same level (up to the number of digits given). On the other hand the calculated differences in total

k -points	$E_{\min} + 5042$ [Hartree]	c_{\min} [Å]
12	-0.3467912 ± 0.0000012	3.8536 ± 0.0060
20	-0.3467640 ± 0.0000008	3.8609 ± 0.0049
30	-0.3467237 ± 0.0000004	3.8591 ± 0.0032
40	-0.3467215 ± 0.0000004	3.8589 ± 0.0034
50	-0.3467184 ± 0.0000004	3.8587 ± 0.0034
60	-0.3467167 ± 0.0000004	3.8589 ± 0.0034

Table 3.1: Coordinates of the minimum in total energy evaluated with respect to different number of k -points. Given errors are associated with the fitting. While the number of k -points influences the total energy the precision of the lattice parameter c_{\min} is mainly limited by other numerical fluctuations to about $\pm 0.1\%$.

energy and in lattice parameter converge to zero with increasing number of k -points (for the total energy graphically presented in Fig. 3.2 or also seen from Table 3.1). The differences are noticeably higher for k -points less than 40. From 40 k -points on (step 3) the change in the total energy related to the higher number of k -points reaches a level of a few μ Hartree. From the data in Table 3.1 we see that the uncertainty concerning the stabilisation of the total energy due to the finite number of k -points exceeds the uncertainty arising from the fitting. At least this is the case for the considered lattice parameter a ($a = 2.75 \text{ \AA}$). It turned out during the calculation of the epitaxial Bain path that $a = 2.75 \text{ \AA}$ exhibits comparatively small errors. Numerical fluctuations are higher for other lattice constants a , leading to an higher error, typically in the order of few μ Hartree. (In Fig. 3.3 on Page 24 we discuss the case $a = 3.20 \text{ \AA}$, where the error is 3×10^{-6} Hartree.)

For the calculation of the epitaxial Bain path we set the number of k -points in each direction to 40. This corresponds to 4531 points in the irreducible part of the Brillouin zone (IBZ). This decision is based on two criteria. The finite number of k -points should stabilise the total energy at the same level of uncertainty as errors due to numerical fluctuations accompany the curve fitting. This is the case for more than 30 k -points. Thus, both uncertainties are in the order of a few μ Hartree. The second reason is physical nature. The Fermi level in palladium happens to fall at a point where the density of states is decreasing rapidly with energy (see Fig. 3.4 on Page 30), making the density of states at the Fermi level $D(E_F)$ sensitive to the Fermi-level position. Thus $D(E_F)$ is sensitive to numerical tolerances. A high number of k -points is necessary for smaller tolerances. As it turned out during our calculation of the total energy along the epitaxial Bain path (see Page 32 et seqq.) we found a range of almost constant total energy, but where it is interesting to know whether the total energy is indeed constant or reveals a structure, i.e. another extremum. Also in this case, a high number

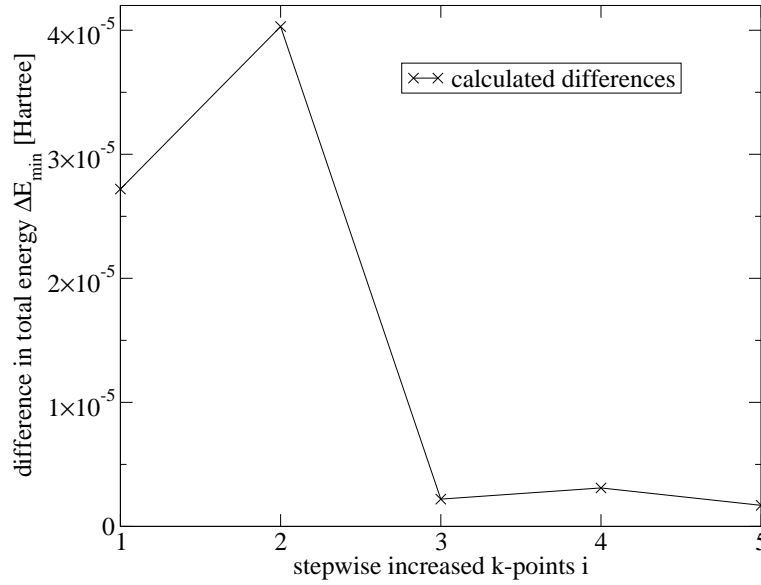


Figure 3.2: To the k -point sampling. The figure shows that the difference in total energy ΔE_{\min} converges to zero with increasing number of k -points. The steps i are defined on Page 20. From step 3 on (increase to 40 k -points) the differences in total energy are significantly smaller.

of k -points is helpful to minimise uncertainties .

In order to estimate to which extend a higher number of k -points than 40 would effect our results (we have to ensure the stability of the total energy at a certain level), we introduced an additional error in the order of magnitude

$$5 \times 10^{-6} \text{ Hartree} \quad (\text{estimated error for total energy due to finite number of } k\text{-points})$$

for the total energy and

$$0.5 \times 10^{-3} \text{ \AA} \quad (\text{estimated error for lattice parameter due to finite number of } k\text{-points})$$

for the lattice parameter, supplementary to the already existing error due to the curve fitting (see Sec. 3.3). This estimation is based on the numbers from Table 3.1. Both errors were added.

This section is closed with a summary of the settings for our calculation with FPLO. These are tabulated in Table 3.2.

3.3 Fitting Methodology and Error Estimation

For our needs some values obtained from band-structure calculations, usually total energies in dependence of a lattice parameter, have to be fitted for further interpretation. This section deals with curve fitting, estimation

Relativistic	scalar relativistic
Exchange-correlation potential	Perdew Wang 92
Convergence condition	density + energy
k -points (k -points in IBZ)	40 40 40 (4531)
Space group	I4/mmm (No. 139)
Wyckoff position	Pd(0,0,0)
Basis	$\underbrace{1s2s2p3s3p3d}_{\text{core}} :: \underbrace{(4s4p)}_{\text{semi-core}} / \underbrace{5s5p4d}_{\text{valence}} +$

Table 3.2: Summarised settings for FPLO5.00-19. IBZ denotes the Irreducible Brillouin Zone.

of errors and the determination of roots of functions. It also gives a short overview of programs used therefor.

The idea behind the error estimation is not to determine the accuracy of the result, i.e. we do not determine how close the calculation is to the true value of the quantity being calculated, since the systematic error of the LDA is not known. Rather we intend to estimate the precision of our calculation, i.e. to determine how well the result has been ascertained.

3.3.1 Least Squares Fit for Energies

The main usage of fitting was to describe the trend of calculated data and to find an analytic representation of the curve. Normally fitting was applied to describe the relation of the total energy in dependence of the out-of-plane lattice parameter c with in-plane lattice parameter a being fixed, $E(a = \text{const}, c)$. The available data from the calculation is discrete and will be denoted in the following by (c_n, E_n) , where $E_n = E(c_n)$ is the calculated total energy at the place c_n . N gives the number of data points available and $n = 1 \dots N$. From the fit to the evaluated energies the coordinates of the minimum c_{EBP} and E_{EBP} for each a will be obtained (in Sec. 3.3.3 on Page 28 we will go into details). This belongs to the second step in the procedure of the calculation of the epitaxial Bain path as characterised on Page 17. In the following we will describe in more detail the fitting methodology and an estimation of errors associated with it.

First of all, an adequate fit function for the mentioned task had to be specified. Since the qualitative relationship between total energy and lattice parameter c around the minimum is expected to be somewhat parabolic for the considered range of values of a , an appropriate fit function is surely a polynomial. Concerning the order of the polynomial the calculated total energies throughout turned out to be analytically well represented by a

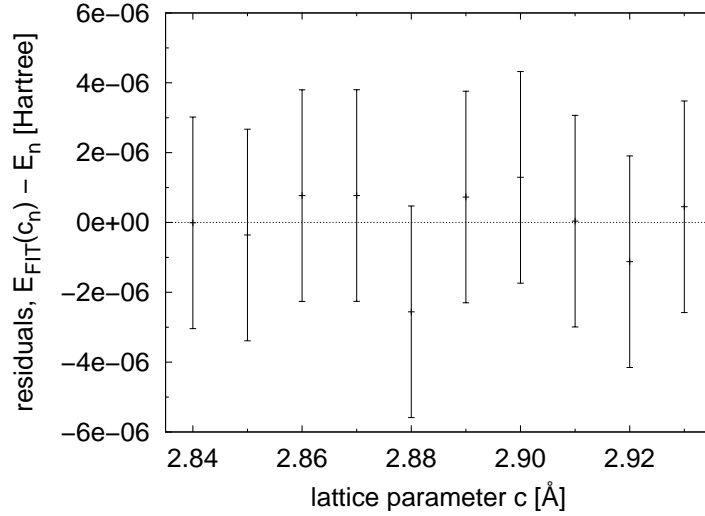


Figure 3.3: For the case $a = 3.20 \text{ \AA}$ we performed a fit to the evaluated total energies E_n . The fit function is a fourth order polynomial and the number of data points equals 10. The graphic shows the residuals of fit function and of the data. Present fluctuations are interpreted to be of numerical origin. The error bars amount to $3 \times 10^{-6} \text{ \AA}$.

polynomial of fourth order in c

$$E_{\text{FIT}}(c) = \sum_{i=0}^4 k_i c^i, \quad (3.1)$$

the $\mathbf{k} = \{k_i\}$, $i = 0 \dots 4$, being the coefficients yet to determine. This user-supplied fit function was the polynomial with the minimum number of parameters modelling the data in good agreement. As an example, in Fig. 3.3 we show for some data, that was fitted by a polynomial of fourth order, the residuals $E_{\text{FIT}}(c_n) - E_n$. Their deviation from zero are interpreted as numerical fluctuations. A rule of thumb is that [33]

$$2\sqrt{N} > M, \quad (3.2)$$

where M is the number of adjustable parameters in the fit function. Our sample size N was fixed to 10 equidistant points. To be in accord with Eq. 3.2 the maximum number of coefficients can be 5 (fourth order polynomial). We compared on the same underlying interval two different kinds of fits, one with 10 sampling points (distance 0.01 \AA) and one with 20 sampling points (distance 0.005 \AA). Both exhibited mean residuals of nearly the same magnitude (deviation 5%), letting us assume that $N = 10$ is an appropriate choice. Although fitting the 20 sampling points with polynomials of higher order (up to six was tested) tended to improve the results of the curve fitting

(mean residuals smaller) we stayed with the polynomial of degree four (and 10 sampling points) due to its good trade-off between goodness-of-fit and simplicity, capturing the regularities in the data adequately and building an appropriate basis for the estimation of errors yet to be introduced.

With the help of the program GNUPLLOT version 4.0 the curve-fitting and the determination of the coefficients k_i was carried out. This program has implemented an iterative least squares Levenberg-Marquardt algorithm [34]. The fitting with GNUPLLOT can be controlled by a parameter named FIT_LIMIT and a number declared for it. This parameter represents the difference in the sum of squared residuals between two interaction steps. The squared residual is the squared deviation between the function value and the input value, evaluated at the same place. In our case

$$\chi^2(\mathbf{k}) = \sum_{n=1}^N \left[\frac{E_{\text{FIT}}(c_n, \mathbf{k}) - E_n}{\sigma_{E,n}} \right]^2, \quad (3.3)$$

where the sum runs over all N data points. In the denominator we have the standard deviation of the calculated total energies. (Let us assume for the moment that there are some normally distributed errors and they are known). When the sum in Eq. (3.3) changes between two iteration steps by a factor less than the declared value for FIT_LIMIT, the fit is considered to have converged. During all usage the value was set to

$$\text{FIT_LIMIT} = 1 \times 10^{-5}.$$

According to [34] “a ‘typical’ value of χ^2 for a ‘moderately’ good fit is”

$$\frac{\chi^2}{N - M} \approx 1. \quad (3.4)$$

The difference $N - M$ represents the degrees of freedom in the fit. Equation (3.4) is a rule of thumb. A too large quotient can be connected with an underestimation of errors or with a wrong fit function (wrong model). Values significantly smaller than 1 point to too large errors or to wrongly determined systematic errors. Unfortunately the errors $\sigma_{E,n}$ associated with the calculated data are not known. In order to assign some error bars to the data we did an estimation of errors according to [34] to which Eq. (3.4) provides a basis. We presumed the errors to be normally distributed and the same for all data points, $\Delta E \equiv \sigma_{E,n}$. We first assigned an arbitrary value to ΔE and minimised χ^2 according to Eq. (3.3), where ΔE takes the place of $\sigma_{E,n}$. (Note that the initial value for ΔE must be small, since the algorithm calculates the differences in χ^2 between two iteration steps and stops if this difference is smaller than a certain number. GNUPLLOT automatically takes care of that.) Finally, after the coefficients have been determined, we recomputed the error ΔE by

$$(\Delta E)^2 = \sum_{n=1}^N \frac{[E_{\text{FIT}}(c_n) - E_n]^2}{N - M}. \quad (3.5)$$

The recomputed error fulfils $\chi^2/(N - M) = 1$ in accord with Eq. (3.4).

The square root of the outcome of Eq. (3.5) would be the error associated with the value of E_{EBP} arising from the fitting of the data using the given model (fourth order polynomial). It will be calculated separately for each a . Additionally we used a confidence level of 95% for the errors so that the error bars assigned to the energies E_{EBP} are $\pm 2\Delta E$ instead of $\pm \Delta E$ for a confidence level of 68%,

$$\Delta E_{\text{EBP}} = 2\Delta E. \quad (3.6)$$

We estimated the error for c_{EBP} from the error ΔE_{EBP} . Therefor we did a Taylor expansion of E_{FIT} around c_{EBP} to second order

$$\begin{aligned} E_{\text{FIT}} \approx & E_{\text{EBP}} + \left. \frac{\partial E_{\text{FIT}}}{\partial c} \right|_{c_{\text{EBP}}} \cdot (c - c_{\text{EBP}}) \\ & + \frac{1}{2} \left. \frac{\partial^2 E_{\text{FIT}}}{\partial c^2} \right|_{c_{\text{EBP}}} \cdot (c - c_{\text{EBP}})^2 + o((c - c_{\text{EBP}})^3) \end{aligned} \quad (3.7)$$

The first derivative vanishes at the minimum. The second derivative can be easily computed from Eq. (3.1). We introduce the abbreviations $\Delta \tilde{E} = |E_{\text{FIT}} - E_{\text{EBP}}|$ and $\Delta \tilde{c} = c - c_{\text{EBP}}$, and we have

$$(\Delta \tilde{c})^2 \approx 2\Delta \tilde{E} \left(\left. \frac{\partial^2 E_{\text{FIT}}}{\partial c^2} \right|_{c_{\text{EBP}}} \right)^{-1}. \quad (3.8)$$

We assume $\Delta \tilde{E}$ to be in the order of ΔE_{EBP} and we reason for the error of c_{EBP} that

$$\Delta c_{\text{EBP}} = (2\Delta E_{\text{EBP}})^{1/2} \left(\left. \frac{\partial^2 E_{\text{FIT}}}{\partial c^2} \right|_{c_{\text{EBP}}} \right)^{-1/2}. \quad (3.9)$$

The outcome of Eq. (3.9) is the error associated to c_{EBP} .

In order to estimate errors of other related variables such as volume and stress, we made use of the propagation of errors formula. The volume per atom along the epitaxial Bain path is given by

$$V_{\text{EBP}}(a) = \frac{a^2 c_{\text{EBP}}(a)}{2}. \quad (3.10)$$

For the error ΔV_{EBP} follows

$$\Delta V_{\text{EBP}} = \left| \frac{\Delta c_{\text{EBP}}}{c_{\text{EBP}}} \right| V_{\text{EBP}}. \quad (3.11)$$

3.3.2 Linear Regression for In-plane Stress

We find for the isotropic in-plane stress σ_{EBP} along the epitaxial Bain path by comparison with Eq. (2.22)

$$\sigma_{\text{EBP}}(a) = \frac{1}{a c_{\text{EBP}}(a)} \left. \frac{\partial E_{\text{EBP}}(a')}{\partial a'} \right|_a. \quad (3.12)$$

For the associated error $\Delta\sigma_{\text{EBP}}$ follows

$$\Delta\sigma_{\text{EBP}} = \left(\left| \frac{\Delta c_{\text{EBP}}}{c_{\text{EBP}}} \right| + \left| \frac{\Delta m_{\text{EBP}}}{m_{\text{EBP}}} \right| \right) \sigma_{\text{EBP}}, \quad (3.13)$$

where we have used the abbreviation $m_{\text{EBP}}(a) = \partial E_{\text{EBP}}(a')/\partial a'|_a$ representing the slope at a along the epitaxial Bain path.

In order to obtain the derivative of the total energy with respect to the in-plane lattice parameter along the epitaxial Bain path, one could fit the total energy with a suitable function. From this fit the derivative and hence the in-plane stress could be evaluated. But using this method makes it difficult, among other things, to take into account the already calculated error of the total energy ΔE_{EBP} and transfer those to the error of the stress.

We decided to proceed in a different way. Instead of fitting the total energy along the epitaxial Bain path, we evaluated the stress by fitting subsets of data points of the total available data to a straight line model (linear regression). In the following we are going to discuss this approach.

Only discrete data is on hand for the epitaxial Bain path, the energy along the epitaxial Bain path and so on. Let us denote one record by $a^{(i)}$, $c_{\text{EBP}}^{(i)}$ and $E_{\text{EBP}}^{(i)}$. The total number of records equals d , so $i = 1 \dots d$. We have calculated errors for our data, denoted by $\Delta c_{\text{EBP}}^{(i)}$ and $\Delta E_{\text{EBP}}^{(i)}$.

We chose a subset L of neighbouring data points (a window) from the total number of data available and performed a linear regression for it. The number of elements in L be l , the first data set in L be j and the last $j+l$. Accordingly, the fit function is a straight line with slope m and axis intercept n

$$E_{\text{EBP}}^{(L)}(a) = m^{(L)} \cdot a + n^{(L)}, \quad (3.14)$$

where the superscript (L) indicates the subset L . This straight line can be considered as an approximation to E_{EBP} at some certain place $\tilde{a}^{(L)}$ (or even some certain interval). The slope of the total energy along the epitaxial Bain path at this certain place $\tilde{a}^{(L)}$ is then approximately

$$\left. \frac{\partial E_{\text{EBP}}(a')}{\partial a'} \right|_{\tilde{a}^{(L)}} \approx m^{(L)}. \quad (3.15)$$

Together with the corresponding lattice constants $c_{\text{EBP}}(\tilde{a}^{(L)})$ we can evaluate the in-plane stress according to Eq. (3.12). Here the calculated $m^{(L)}$ replaces the derivative in Eq. (3.12) at this certain $\tilde{a}^{(L)}$

$$\sigma_{\text{EBP}}(\tilde{a}^{(L)}) \approx \frac{1}{\tilde{a}^{(L)} c_{\text{EBP}}(\tilde{a}^{(L)})} m^{(L)}. \quad (3.16)$$

Which is the best $\tilde{a}^{(L)}$ to choose? It is best to evaluate the mean of all $a^{(i)}$'s of the subset L and assign the slope to that value [35]

$$\tilde{a}^{(L)} = \sum_{i=j}^{j+l} \frac{a^{(i)}}{l}, \quad a^{(i)} \in L. \quad (3.17)$$

If the subset has an odd number of elements, the mean equals one of the $a^{(i)}$'s from the subset L (we have to presume equidistant values for the $a^{(i)}$'s). But only if the mean is one of the $a^{(i)}$'s from L the associated values $c_{\text{EBP}}^{(i)}$ and $\Delta c_{\text{EBP}}^{(i)}$ are already known.

Under this circumstances, for each subset L holds

$$a^{(k)} \equiv \tilde{a}^{(L)} \quad \text{and} \quad a^{(k)} \in L, \quad (3.18)$$

and we finally assign the evaluated stress to the data set k

$$\sigma_{\text{EBP}}^{(k)} \equiv \frac{1}{a^{(k)} c_{\text{EBP}}^{(k)}} m^{(L)}. \quad (3.19)$$

At this point we would like to summarise the presented idea. In principle we evaluated the in-plane stress for the data set k by a linear regression of data taken from a subset of the total data, namely the sets $j, j+1, \dots, k, k+1, \dots, j+l$. The linear regression provided an approximation to the slope of $E_{\text{EBP}}(a)$ at some certain place in terms of the variable $m^{(L)}$. We argued that the slope is best assigned to the place $a^{(k)}$, whereat $a^{(k)}$ is the mean of all $a^{(i)}$'s in L . In this way we evaluated the in-plane stress $\sigma_{\text{EBP}}^{(k)}$ for the data set k . In order to obtain the in-plane stress for all records i we had to repeat the mentioned procedure for all subsets L , i.e. all combinations of l neighbouring values of the $a^{(i)}$. The number of elements in L is fixed of course.

Concerning the linear regression algorithm, we implemented a code according to [34]. The linear regression worked such, that errors for $m^{(L)}$ and $n^{(L)}$ will be available after the regression was done. That allowed us to calculate an error for the in-plane stress according to Eq. (3.13). However, we forwent the calculation of the errors of the stress in this work, because the main interest was directed at its principal trend. Depending on the window l the regression tends to smooth the data more or less. In Sec. 3.5.5 we will compare two stress curves, one with $l = 3$ and the second with $l = 5$.

3.3.3 Root Finding

Once we have approximated the calculated total energies with a suitable fit function $E_{\text{FIT}}(c)$, we are able to determine the coordinates of its minimum, c_{EBP} and E_{EBP} . It is clearly a similar task to find the roots of the derivative of the fit function with respect to c

$$\left(\frac{\partial E_{\text{FIT}}(c)}{\partial c} \right) \Big|_{c_{\text{EBP}}} = 0. \quad (3.20)$$

The derivative of Eq. (3.1) is a polynomial of third order in c and the root(s) can be gained by analytical methods. Nevertheless there exists a variety of

algorithms which determine roots numerically, which is also indispensable for the request of automation. We implemented an algorithm in C++ based on the iterative Newton-Raphson method. The kernel of our program was taken from [34]. In contrast to the original program the data type of all floating point variables was throughout changed from `FLOAT` to `DOUBLE`. Newton's method requires both the function and its derivative, thus the first and second derivatives of E_{FIT} with respect to c . Both derivatives were computed analytically. The precision of the result can be given a limit. We refined the value for the root until its precision was known within 1×10^{-5} Å. We neglected errors associated with the numerical determination of c_{EBP} and E_{EBP} . Surely numerics is an error source, for instance due to the limited precision of floating point variables. But since its order of magnitude is much smaller than i.e. the errors from the fitting itself, we discarded them. The values for the roots are precise to 1×10^{-5} Å which is two orders of magnitude smaller than the typical values for Δc_{EBP} .

3.4 States With Cubic Symmetry

We know from the properties of the epitaxial Bain path that it represents a transformation between the bcc and the fcc structure (Sec. 2.2). What we are interested in here is to determine only the two states, which indeed belong to the epitaxial Bain path and which have cubic symmetry (i.e. the bcc and the fcc structure), but without calculating the epitaxial Bain path itself. We will do this, metaphorically speaking, by moving along the two straights that indicate the cubic structures in Fig. 2.2 on Page 9. Along both lines we determine again the minimum in energy. The result will be two cubic structures, that are stress free, and which are situated in the intersection points with the epitaxial Bain path. In the case of fcc, we determine the numerical ground state lattice constant.

3.4.1 Fcc Bravais lattice

At first we wanted to reproduce the experimental lattice parameter of palladium, as it occurs in the fcc structure in nature. Therefore we did total energy calculations with the settings given in Table 3.2 on Page 23, the space group being the only exception which is now $\text{Fm}\bar{3}\text{m}$ (No. 225) and suitable for the fcc structure. The lattice parameter was varied around the experimental lattice constant $c_{\text{exp}}^{\text{fcc}}$. From the fit to the evaluated energies we determined the minimum, denoted by $c_{\text{num}}^{\text{fcc}}$, which is the numerical LDA ground state lattice constant of palladium, and the corresponding total energy $E_{\text{fcc}} = E(c_{\text{num}}^{\text{fcc}})$

$$\begin{aligned} c_{\text{num}}^{\text{fcc}} &= (3.876 \pm 0.003) \text{ \AA} \\ E_{\text{fcc}} &= (-5\,042.346\,698 \pm 0.000\,006) \text{ Hartree} \end{aligned}$$

This value is around 0.4% smaller than the experimental value $c_{\text{exp}}^{\text{fcc}} = 3.890 \text{ \AA}$. This deviation is typical for the LDA [20].

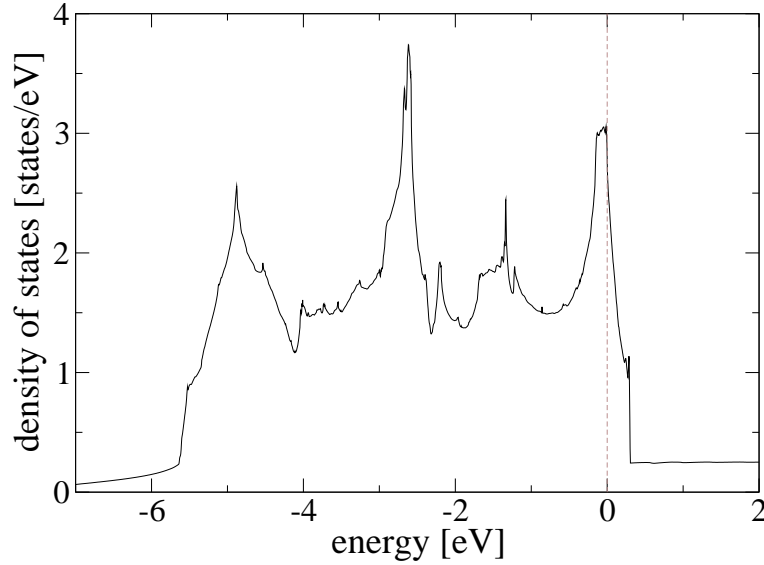


Figure 3.4: Density of states per atom of fcc palladium. A large peak in the density of states is located just below the Fermi level. The density of states at the Fermi level is 2.76 states/eV.

At this point we decided to test whether the same result for the minimum will be obtained, if we use the space group for the ct Bravais lattice, $I4/mmm$ (No. 139), instead, but leave all other settings unchanged (that is the space group we used for the calculation of the epitaxial Bain path). Of course, c and a are connected via the ratio $\sqrt{2}$. From the physical point of view we describe exactly the same structure and the same symmetries as above, but treat the fcc lattice numerically in a different way. With this settings the result is slightly distinct from before (minimum $c_{\text{num}}^{\text{ct}}$ and $E_{\text{ct}} = E(c_{\text{num}}^{\text{ct}})$)

$$\begin{aligned} c_{\text{num}}^{\text{ct}} &= (3.877 \pm 0.002) \text{ \AA} \\ E_{\text{ct}} &= (-5\,042.347\,726 \pm 0.000\,006) \text{ Hartree,} \end{aligned}$$

expressing, that numerics due to the choice of the space group has a small influence on the result.

In Fig. 3.4 we show the density of states per atom for fcc palladium with the characteristic peak just below the Fermi level.

3.4.2 Bcc Bravais lattice

In the same fashion as for the fcc structure we determined the minimum of the bcc structure. The relevant space group is $Im\bar{3}M$ (No. 229) and again all

other settings were as stated in Table 3.2. The lattice parameter was varied within the interval $3.04 \text{ \AA} \leq c \leq 3.13 \text{ \AA}$. The minimum value and associated energy are denoted $c_{\text{num}}^{\text{bcc}}$ and E_{bcc} , respectively, and were evaluated to

$$\begin{aligned} c_{\text{num}}^{\text{bcc}} &= (3.083 \pm 0.008) \text{ \AA} \\ E_{\text{bcc}} &= (-5\,042.345\,128 \pm 0.000\,019) \text{ Hartree.} \end{aligned}$$

The cross-check with the space group $I4/mmm$ and $c = a$ now yielded exactly the same result (minimum $\tilde{c}_{\text{num}}^{\text{ct}}$ and $\tilde{E}_{\text{ct}} = E(c_{\text{num}}^{\text{ct}})$)

$$\begin{aligned} \tilde{c}_{\text{num}}^{\text{ct}} &= (3.083 \pm 0.008) \text{ \AA} \\ \tilde{E}_{\text{ct}} &= (-5\,042.345\,128 \pm 0.000\,019) \text{ Hartree.} \end{aligned}$$

In Fig. 3.5 we show the density of states for bcc palladium.

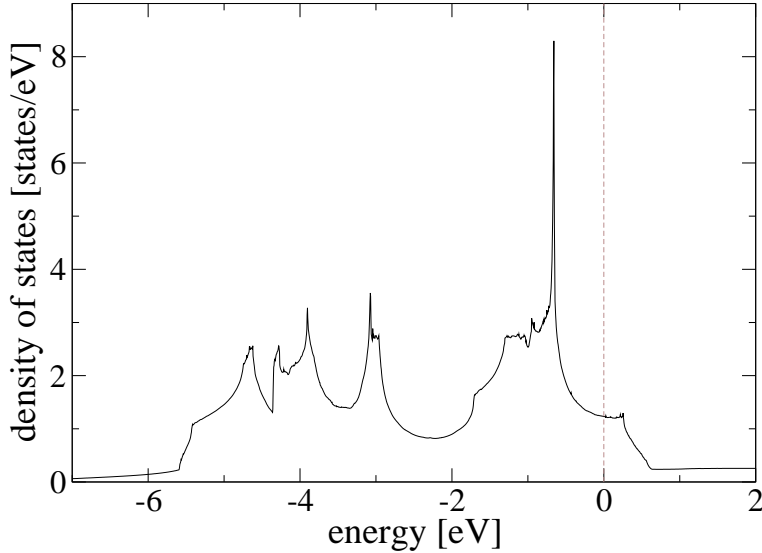


Figure 3.5: Density of states per atom of bcc palladium. 1.23 states/eV are found at the Fermi level. This kind of shape of the curve is typically found among bcc transition metals.

3.5 Results and Discussion

In this section we present the results of our calculation for palladium. Different physical quantities of interest will be analysed and interpreted along the epitaxial Bain path. Thus, these quantities appear as a function of the in-plane lattice parameter a . The underlying range of a is $2.50 \text{ \AA} \leq a \leq 3.50 \text{ \AA}$.

3.5.1 Total Energy Along Epitaxial Bain Path

In Fig. 3.6 on Page 33 we show the total energy as a function of the lattice parameter a along the epitaxial Bain path, $E_{\text{EBP}}(a)$. For purposes of clarity the axis of abscissae was limited to the range $2.55 \text{ \AA} \leq a \leq 3.40 \text{ \AA}$, because outside this interval the total energy rises strongly. The axis of ordinates gives the total energy relative to the lowest energy value along the curve, E_{ct} , whose value we have stated on Page 29.

The global minimum of the curve at around 2.741 \AA ($\approx c_{\text{num}}^{\text{ct}}/\sqrt{2}$) corresponds to the fcc ground state. In the range $3.04 \text{ \AA} \leq a \leq 3.18 \text{ \AA}$ the total energy is almost constant. An image detail of this range is shown in Fig. 3.8 on Page 35, where we see more clearly that the total energy indeed stabilises at a level constant within the error bars of around 1.6×10^{-3} Hartree above E_{ct} . The bcc structure at around 3.08 \AA is located in that area.

We discussed in Sec. 2.2 the properties of the epitaxial Bain path and mentioned, that the total energy must have a vanishing first derivative in the total energy along the epitaxial Bain path with respect to the parameter a at structures of cubic symmetry. Clearly this is the case for the fcc structure. The bcc structure is located just within the range of constant total energy. We interpret the trend in the total energy to have an horizontal inflexion point in the respective range.

We think that the small hump at around 2.82 \AA is of physical origin. Its occurrence coincides with a change in the band structure which is object of discussion in Sec. 3.5.4.

At this point we would like to emphasise an experiment by Jona and coworkers [36], who reported to have coherently grown a thin layer of Pd on W{001}. Pd was grown with in-plane lattice constant $\approx 3.17 \text{ \AA}$. This corresponds to an elongation of about 15% compared to the ground state.

3.5.2 Epitaxial Bain Path

In Fig. 3.7 on Page 34 we show what we defined as the epitaxial Bain path in the tetragonal plane, namely a transition between the bcc and fcc structure via tetragonal distortions. For each a we calculated the particular lattice parameter c_{EBP} at which the out-of-plane stress vanishes. As well as for the total energy the axis of abscissae was limited to $2.55 \text{ \AA} \leq a \leq 3.40 \text{ \AA}$. By dashed grey lines we indicated the configurations with cubic symmetry.

3.5.3 Relative Volume Along Epitaxial Bain Path

The volume per atom along the epitaxial Bain path $V_{\text{EBP}}(a)$ was given by Eq. (3.10) on Page 26. Instead of the volume per atom, the relative volume per atom $V_{\text{EBP}}/V_{\text{fcc}}$ is plotted in Fig. 3.9 on Page 36. The divisor V_{ct} is the volume of the state that has the lowest total energy along the epitaxial Bain

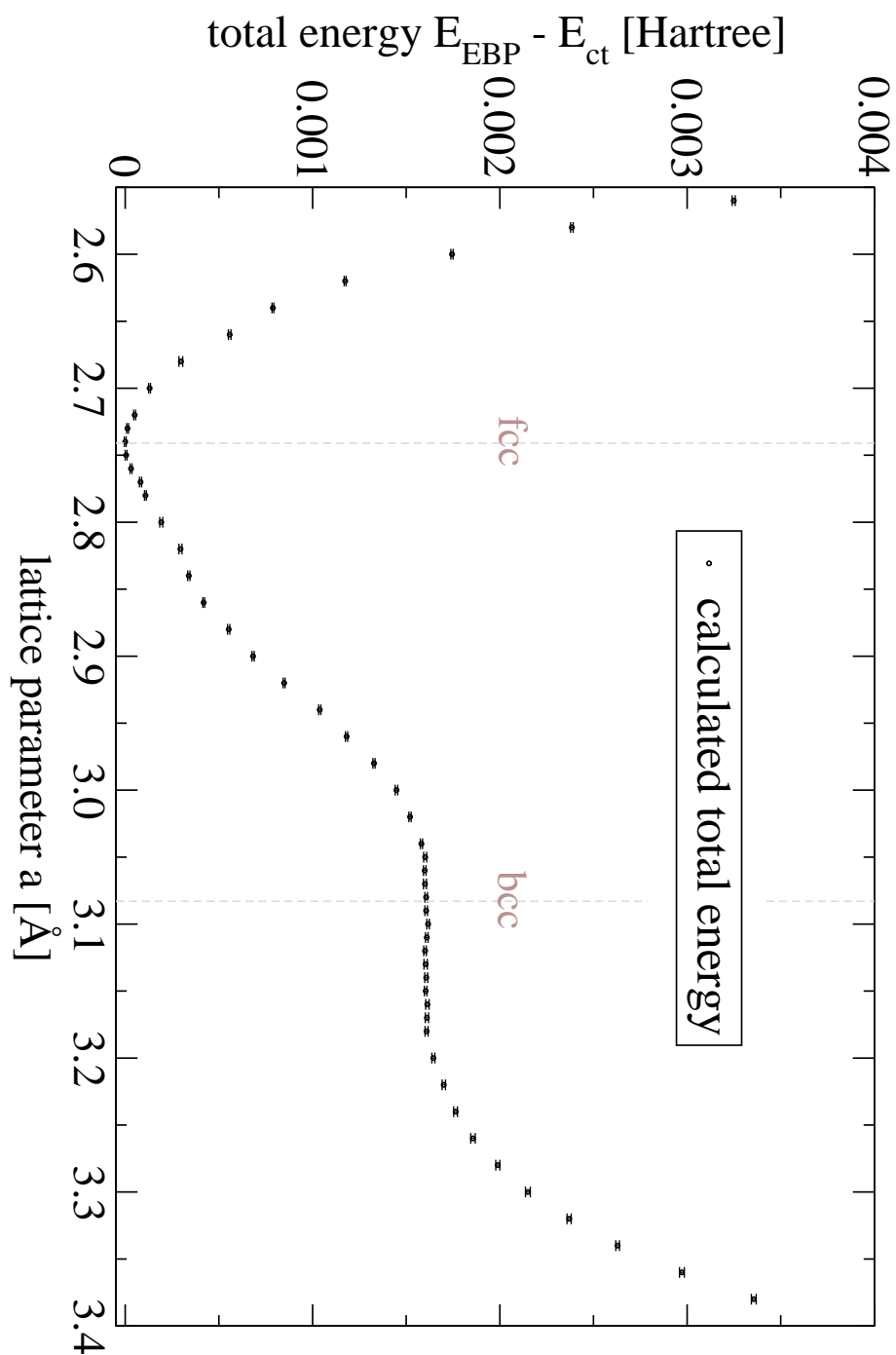


Figure 3.6: The total energy per atom of palladium along the epitaxial Bain path. The energy is given relative to the lowest calculated energy E_{ct} . The fcc ground state is at around 2.741 \AA . In the range $3.04 \text{ \AA} \leq a \leq 3.18 \text{ \AA}$ the total energy does almost not change. An image detail of this region is shown in Fig. 3.8.

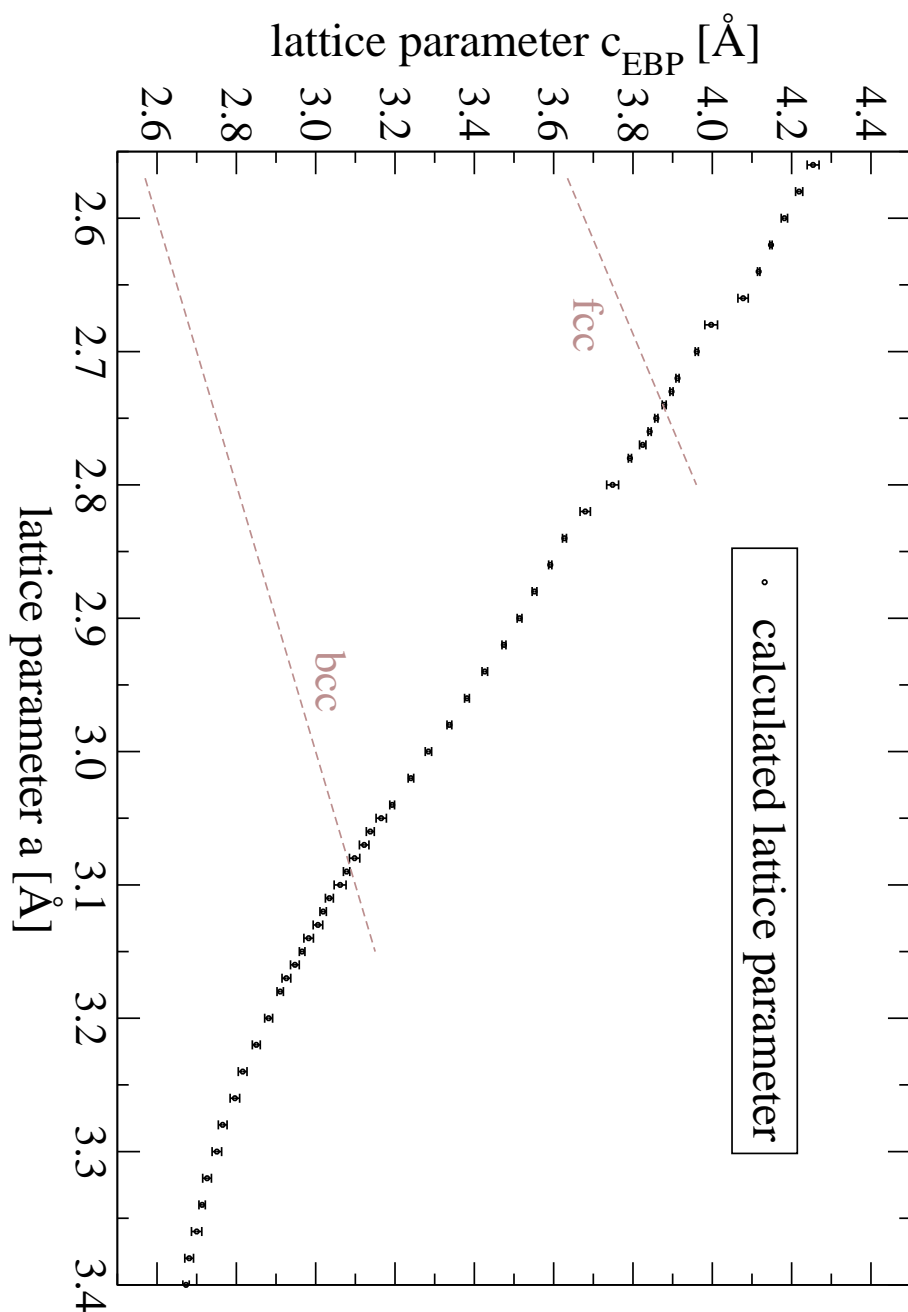


Figure 3.7: The epitaxial Bain path of palladium in the tetragonal plane. Lattice configurations (a, c) that represent cubic symmetry are indicated by grey dashed lines. At intersection points of the straights and the EBP we find cubic structures that are stress-free and extremal in total energy.

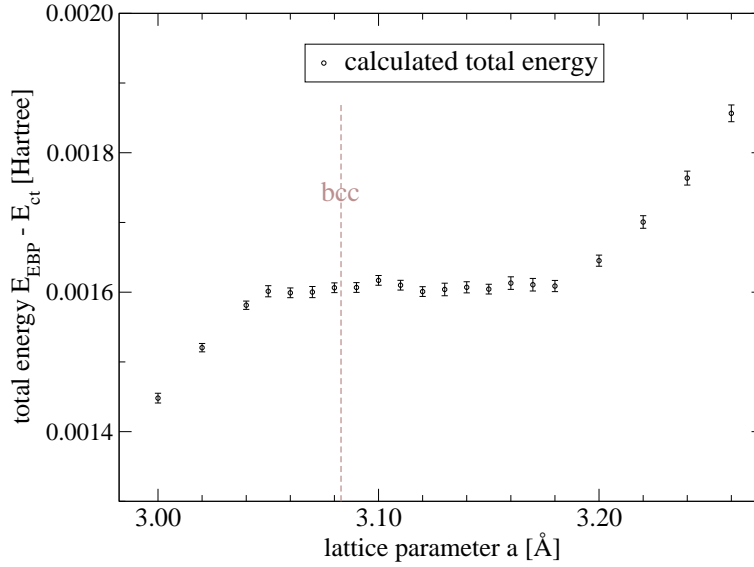


Figure 3.8: This figure shows a detailed image from Fig. 3.6. The total energy per atom remains at a level constant within the error bars for a range of lattice parameters a .

path E_{ct} (the equilibrium volume). Its value is

$$V_{ct} = \frac{(c_{num}^{ct})^3}{4} = 14.569 \text{ \AA}^3.$$

The experimental equilibrium volume V_{exp}^{fcc} is

$$V_{exp}^{fcc} = \frac{(c_{exp}^{fcc})^3}{4} = 14.716 \text{ \AA}^3.$$

The calculation underestimates the experimental value by approximately 1%. Figure 3.9 shows that the volume per atom changes only little ($< 2\%$) when following the epitaxial Bain path from the fcc to the bcc structure. The volume curve shows a shallow minimum around the bcc structure.

3.5.4 Density of States Along Epitaxial Bain Path

The introduction already pointed out that one is very interested in palladium due to its incipient magnetic properties. The onset of magnetic behaviour has been predicted at an isotropic expansion of the lattice parameter by few percent. The states which belong to the epitaxial Bain path exhibit distortions of a different kind, but lead to a rather small increase in volume per atom, as we depicted before. Nevertheless the atomic arrangement is essentially modified.

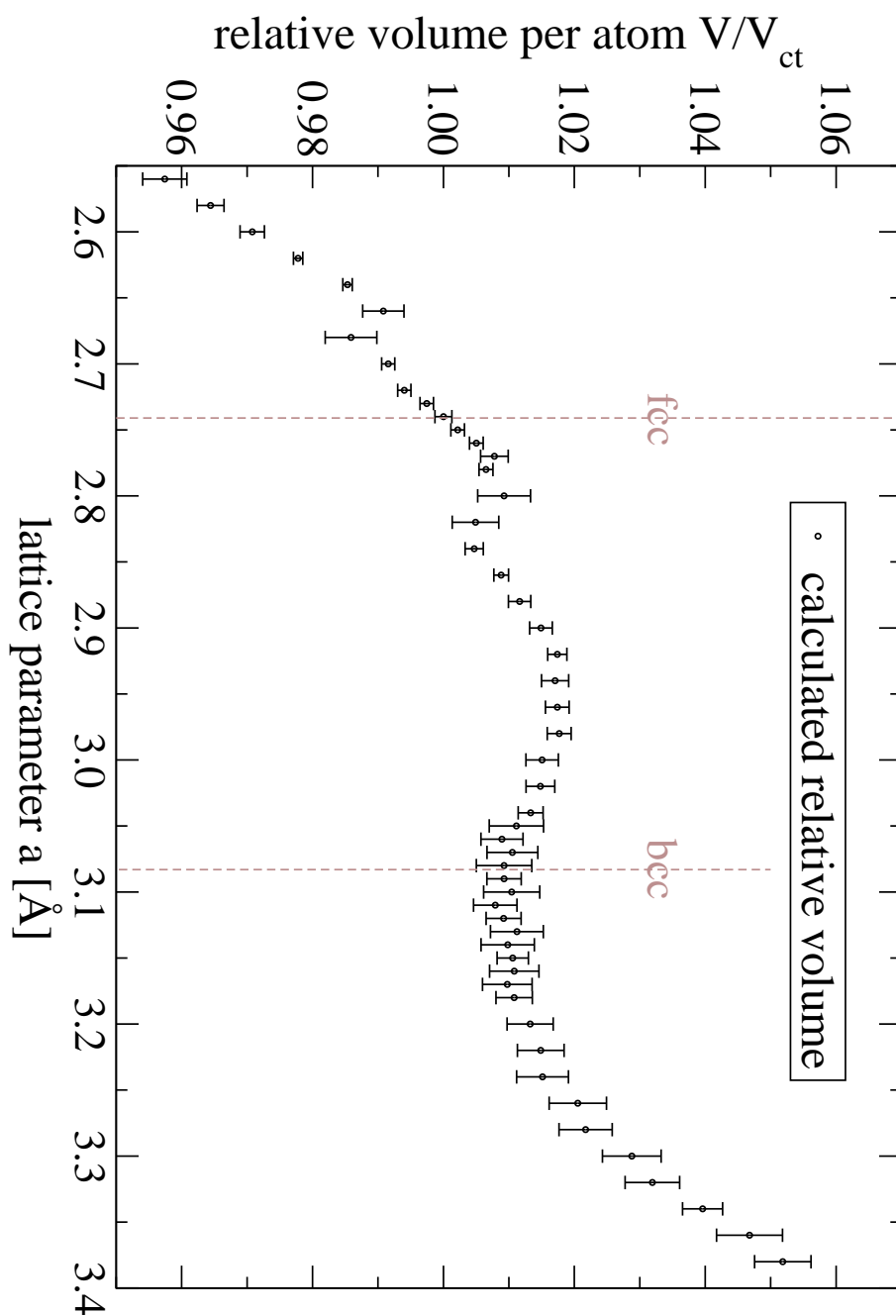


Figure 3.9: The relative volume per atom V/V_{ct} along the epitaxial Bain path. The volume V_{ct} is the volume of the state that has the lowest total energy (ground state). There is a small change in volume along the transition from the fcc to the bcc structure.

In Sec. 2.4 we introduced the Stoner criterion as a sufficient criterion for a ferromagnetic instability. Here we will make use of it. We are interested in how the product of the density of states taken at the Fermi level and the Stoner parameter changes along the epitaxial Bain path. Thus we actually need to evaluate both quantities. We already pointed out in Sec. 2.4 that the density of states is the more important factor, because it is more sensitive to the crystal structure [6, 29]. In contrast to the density of states the Stoner parameter is rather insensitive to the crystal structure and in a good approximation constant for all configurations of the epitaxial Bain path. Thus it is more worthy (and much simpler) to investigate the behaviour of the density of states at the Fermi level, $D(E_F)$, since one expects more pronounced effects there. The density of states per atom along the epitaxial Bain path is shown in Fig. 3.10 on Page 3.10. At first glance we notice that the highest number of states per unit energy comes along with the fcc ground state of palladium. Rather quickly the density of states falls off in the nearby vicinity of the ground state. At the lattice parameter associated with the bcc structure the density of states reaches a minimum. On the basis of Fig. 3.10 we conclude that the Stoner criterion is not fulfilled for any configuration of the epitaxial Bain path, since the Stoner criterion is not fulfilled for the ground state which exhibits the highest density of states. For the ground state the Stoner product was calculated to 0.78 [6, 8].

Eye-catching are some unsteadinesses in the trend of the curve in Fig. 3.10. Noticeable are peaks in the density of states, most pronounced at a equal 2.84 Å, at 3.22 Å and less striking at 2.64 Å. A closer look on the band structure at respective points reveals the reason for the peaks. Exemplarily for all three cases we consider the peak at 2.84 Å. We show a section of the band structure for 2.84 Å and the corresponding density of states in Fig. 3.11 on Page 39. A change in the band structure between the points **X** and **P** is the underlying reason for the peak in the density of states. A flat band slips below the Fermi level at $a = 2.84$ Å. A figure of the Brillouin zone of the centred tetragonal lattice with indicated symmetry points is given in App. C.

3.5.5 In-plane Stress Along Epitaxial Bain Path

Figure 3.12 on Page 41 compares two in-plane stress curves along the epitaxial Bain path $\sigma_{EBP}(a)$. The interval of a is limited to [2.65 Å, 3.30 Å]. The stress is given in units of GPa. Both curves have in common that stress free states are found at places where the derivative of the total energy with respect to the lattice parameter a vanishes. These places are the fcc ground state and a range close to the bcc structure, where the total energy remains at a constant level.

According to our description of the calculation of the in-plane stress on Page 26 et seqq. the values for a must be equidistant. However the original

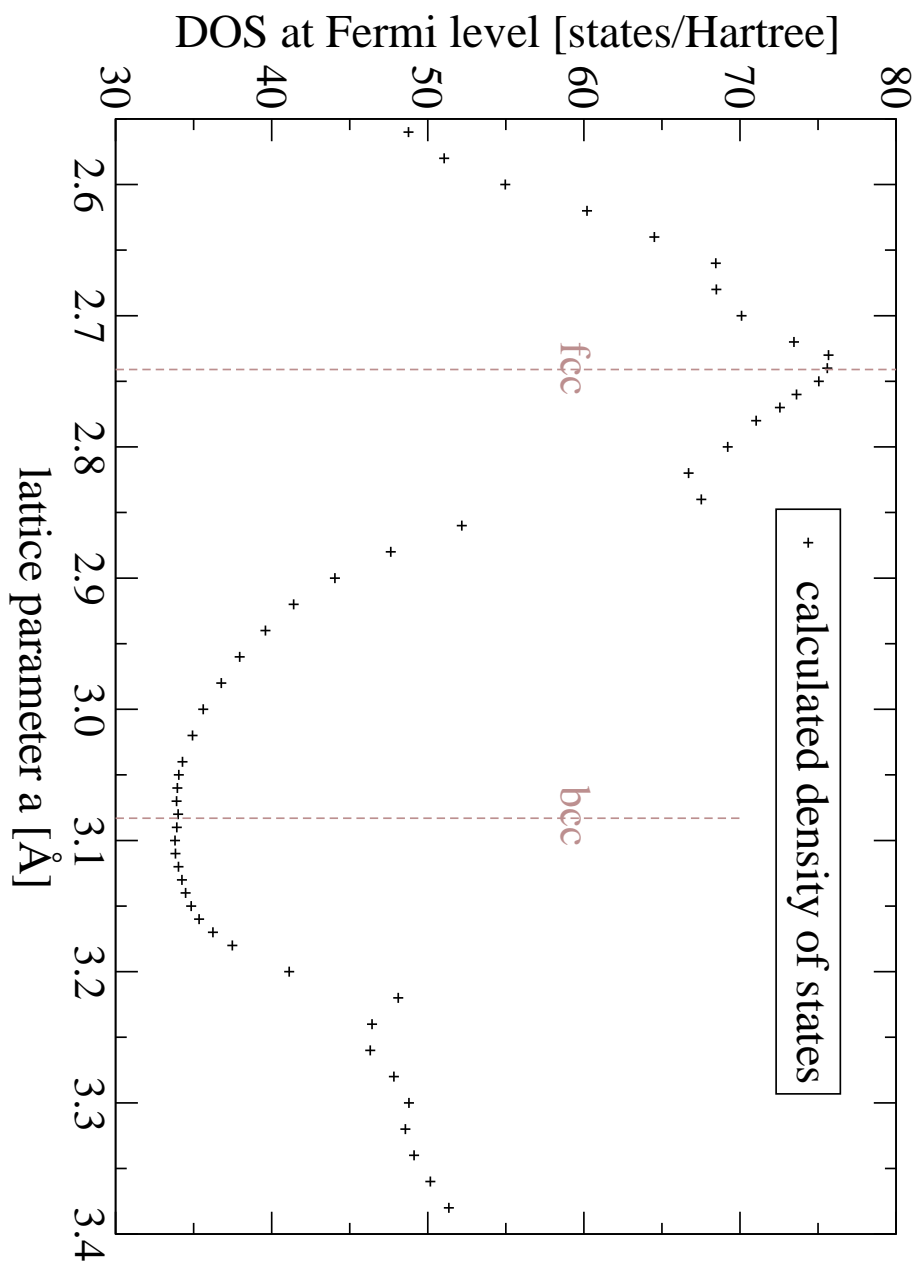
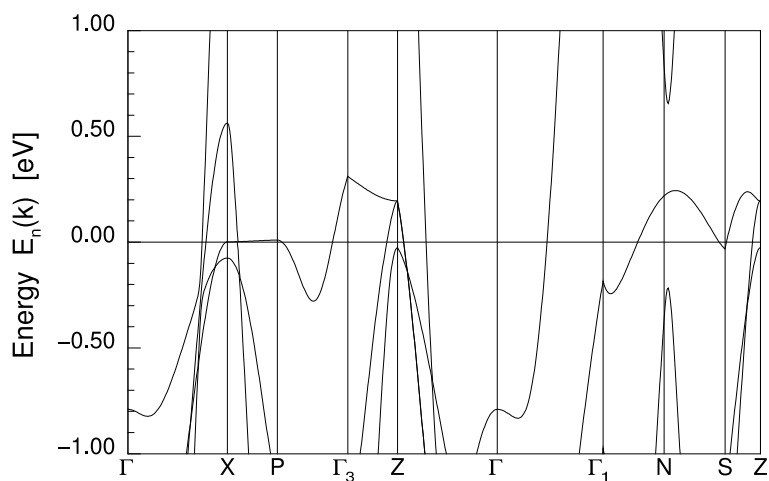
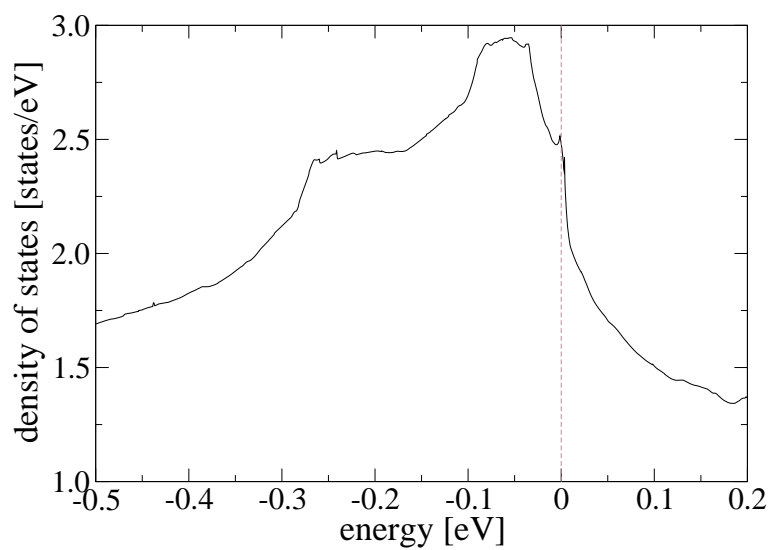


Figure 3.10: Density of states per atom of palladium at the Fermi level along the epitaxial Bain path. The fcc ground state exhibits the highest DOS. The origin of noticeable peaks, for instance at $a = 2.84$ Å, is explained in the text.



(a) band structure



(b) density of states

Figure 3.11: Origin of the peak in the density of states at the Fermi level at $a = 2.84 \text{ \AA}$. A flat band between **X** and **P** causes the peak in the density of states.

data was not, because we had chosen some additional intermediate values within the otherwise equidistant grid of a . For the calculation of the stress we neglected the intermediate values. The linear regression was done for two different numbers of neighbouring data points l (window), namely for $l = 3$ and $l = 5$. Both curves in Fig. 3.12 show similarities at regions of comparatively small curvature. The curves are distinct at regions of high curvature, because the curve with $l = 5$ smoothes the data to a greater extent.

3.6 Comparison

In this section we compare our work with a similar calculation of Jona and Marcus [14]. They used the band structure scheme WIEN97 [37] with 12000 k -points in total or 828 k -points¹ in the irreducible part of the Brillouin zone (our work 64000 in total or 4531 k -points in the irreducible part). Jona and Marcus calculated the epitaxial Bain path of palladium with both the local density approximation and the generalised gradient approximation (GGA).

In Fig. 3.13 we present a comparison between both calculations. The total energy along the epitaxial Bain path is here drawn as a function of the axial ratio c/a . Note that the unit of the total energy is Rydberg. Jona and Marcus reported the bcc structure at a maximum in total energy at $c/a = 1$ and a shallow minimum at $c/a = 0.916$, which is about 3.5 mRy higher than the minimum of the fcc phase ($c/a = \sqrt{2}$). We found for that value 3.2 mRy. This second minimum at $c/a = 0.916$ is about 0.2 mRy deep. This is in contrast to our work, because we did not find the second minimum (and hence no maximum at $c/a = 1$, but rather a range of constant energy within the error bars (this range is within $0.91 \leq c/a \leq 1.04$). The order of magnitude of the calculated errors in this range is about $5 \mu\text{Hartree}$ and so much smaller than the depth of the minimum found by Jona and Marcus.

¹private communication

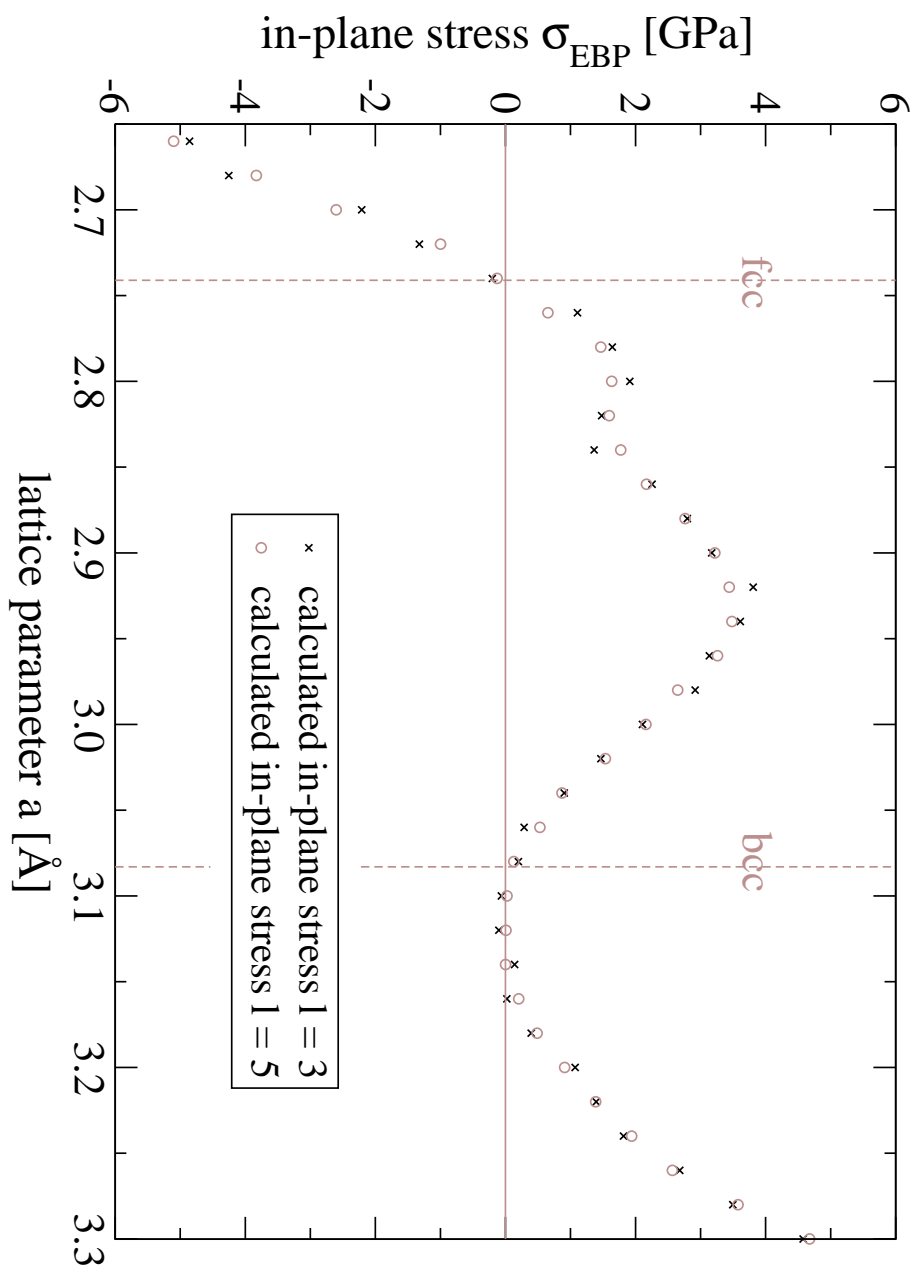
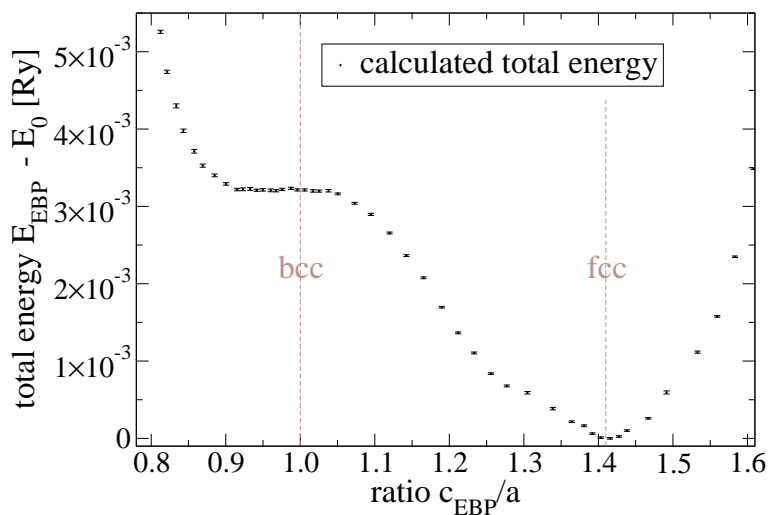
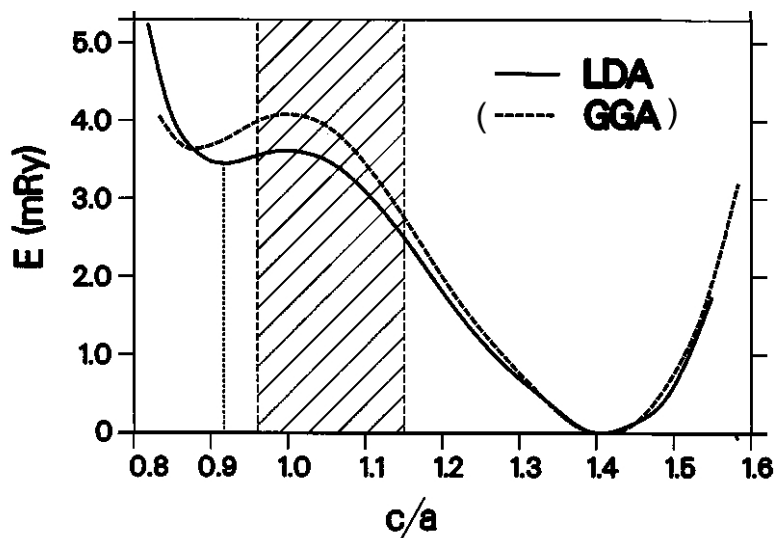


Figure 3.12: In-plane stress [(001) plane] along the epitaxial Bain path obtained from piecewise linear regression of available data for two different numbers of neighbouring data points l .



(a) Our work



(b) Work by Jona and Marcus

Figure 3.13: Comparison of LDA calculations for the total energy along the epitaxial Bain path of palladium. The hatched area in (b) marks the interval c/a where the curvature of $E_{EBP}(a)$ is negative – Eq. (2.32) is not fulfilled and states within this range are unstable.

Chapter 4

Summary and Outlook

In this work we calculated by means of density functional theory in the local density approximation the epitaxial Bain path of bulk palladium. The epitaxial Bain path incorporates strained tetragonal structures and defines a transition between the fcc and the bcc structure. Heteroepitaxial growth on (001) cubic substrates results in such strained structures due to lattice mismatch. The knowledge of the epitaxial Bain path allowed us to investigate different physical properties of palladium along this special path. The principal property of interest was the tendency of palladium towards a ferromagnetic instability. We investigated this by means of the Stoner criterion. Our calculations showed that the density of states at the Fermi level significantly decreases for any considered states compared to the one of the fcc ground state. Hence we reasoned that there is no indication for a ferromagnetic instability. We also computed the planar stress, the total energy and the volume along the epitaxial Bain path.

The non-equilibrium bcc structure is found in a stress-free state at a total energy of about 1.6 mHartree higher than the fcc ground state. The bcc structure is situated in a region where the total energy is constant within the error bars along the epitaxial Bain path. In this respect, our calculation disagrees with a comparable calculation of Jona and Marcus [14] who reported the bcc structure in a local maximum in total energy and additionally found a tetragonal structure locally minimal in total energy.

Within this work we gave an estimation of numerical errors associated with our calculation. Uncertainties arised from the fitting of data with numerical noise, in particular from a finite number of k -points. All calculated quantities but the stress were given with a corresponding error.

A possible extension of this work would be the calculation of the epitaxial Bain path of palladium using the generalised gradient approximation for further comparison with [14] and the application of a direct calculation of forces for the determination of in-plane stress.

Appendix A

Representation of Exchange-correlation Potential

In the parametrisation according to Perdew and Wang [24], the exchange-correlation energy per particle (or exchange-correlation density) ϵ_{xc} is split into the exchange energy density e_x and the correlation energy density e_c

$$e_{xc} = e_x + e_c \quad (\text{A.1})$$

with

$$e_x = -\frac{3}{4\pi} \frac{(9\pi/4)^{\frac{1}{3}}}{r_s} \quad (\text{A.2})$$

and

$$e_c = -2c_0 (1 + \alpha_1 r_s) \ln \left[1 + \frac{1}{2c_0(\beta_1 r_s^{\frac{1}{2}} + \beta_2 r_s + \beta_3 r_s^{\frac{3}{2}} + \beta_4 r_s^2)} \right], \quad (\text{A.3})$$

where

$$\beta_1 = \frac{1}{2c_0} \exp\left(-\frac{c_1}{2c_0}\right), \quad (\text{A.4})$$

$$\beta_2 = 2c_0 \beta_1^2. \quad (\text{A.5})$$

The α_1 , β_3 , β_4 , c_0 and c_1 are coefficients stated in [20, 24] and r_s is the Wigner-Seitz radius

$$r_s = \left(\frac{3}{4\pi n}\right)^{\frac{1}{3}}. \quad (\text{A.6})$$

Appendix B

Restriction on Elastic Constants

The strain energy W per unit volume V_0 of a crystal is [38]

$$\frac{W}{V_0} = \frac{1}{2} \sum_{ij} c_{ij} \epsilon_i \epsilon_j \quad (i, j = 1 \dots 6), \quad (\text{B.1})$$

with the components of the elastic stiffness tensor c_{ij} and those of the strain tensor ϵ_i . Shorthand notation was used. Required for the stability of a crystal is positive strain energy, that means the quadratic form in Eq. (B.1) must be positive definite for all real values of the ϵ_i (unless all ϵ_i are zero). The necessity of positive strain energy implies restrictions on the elastic constants. The necessary and sufficient condition on the matrix $C = (c_{ij})$ of the elastic constants to be positive definite are, that the determinant of the matrix C and all minor determinants which have common diagonal elements with C , must be positive. The tetragonal classes $4mm$, $\bar{4}2m$, 422 and $4/mmm$ have six independent elastic constants c_{11} , c_{12} , c_{13} , c_{33} , c_{44} and c_{66} . C is symmetric and explicitly denoted

$$C = \left(\begin{array}{ccc|ccc} c_{11} & c_{12} & c_{13} & 0 & 0 & 0 \\ c_{12} & c_{11} & c_{13} & 0 & 0 & 0 \\ c_{13} & c_{13} & c_{33} & 0 & 0 & 0 \\ \hline 0 & 0 & 0 & c_{44} & 0 & 0 \\ 0 & 0 & 0 & 0 & c_{44} & 0 \\ 0 & 0 & 0 & 0 & 0 & c_{66} \end{array} \right). \quad (\text{B.2})$$

Accordingly, we find from entries in the diagonal that

$$c_{11} > 0, \quad c_{33} > 0, \quad c_{44} > 0, \quad c_{66} > 0. \quad (\text{B.3})$$

From the determinant of the upper left 3 by 3 block matrix we require two more conditions

$$c_{11} > |c_{12}| \quad (\text{B.4})$$

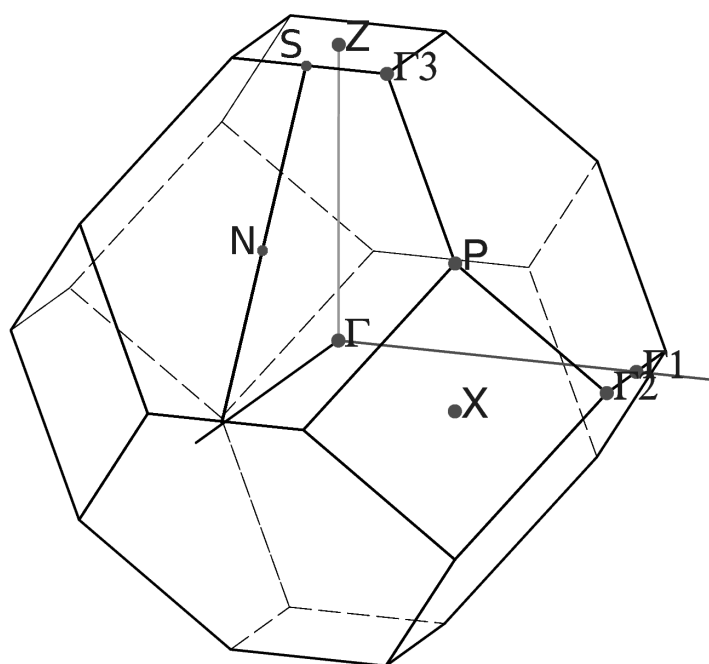
$$c_{33} (c_{11} + c_{12}) > 2c_{13}^2. \quad (\text{B.5})$$

There is an additional condition from the same minor determinant, $c_{33}c_{11} > c_{13}^2$, which is always fulfilled if Eqs. (B.4) and (B.5) hold and therefore redundant. Eventually must be $\det[C] > 0$ which is readily seen to be the case if conditions (B.3), (B.4) and (B.5) are satisfied

$$\det[C] = (c_{33} (c_{11} + c_{12}) - 2c_{13}^2) (c_{11} - c_{12}) c_{44}^2 c_{66} > 0. \quad (\text{B.6})$$

Appendix C

Brillouin Zone



Bibliography

- [1] P. Hohenberg and W. Kohn, Phys. Rev. **136**, B864 (1964).
- [2] W. Kohn and L. J. Sham, Phys. Rev. **140**, A1133 (1965).
- [3] A. M. Clogston et al., Phys. Rev. **125**, 541 (1962).
- [4] F. M. Mueller, A. J. Freeman, J. O. Dimmock, and A. M. Furdyna, Phys. Rev. B **1**, 4617 (1970).
- [5] H. Chen, N. E. Brener, and J. Callaway, Phys. Rev. B **40**, 1443 (1989).
- [6] J. F. Janak, Phys. Rev. B **16**, 255 (1977).
- [7] P. Larson, I. I. Mazin, and D. J. Singh, Phys. Rev. B **69**, 064429 (2004).
- [8] *Magnetische Schichtsysteme in Forschung und Anwendung*, Materie und Material / Matter and Materials, Forschungszentrum Jülich GmbH, 1999.
- [9] L. Fritsche, J. Noffke, and H. Eckardt, J. Phys. F: Met. Phys. **17**, 943 (1978).
- [10] V. L. Moruzzi and P. M. Marcus, Phys. Rev. B **39**, 471 (1989).
- [11] V. L. Moruzzi, Phys. Rev. Lett. **57**, 2211 (1986).
- [12] G. A. Prinz, Phys. Rev. Lett. **54**, 1051 (1985).
- [13] P. Alippi, P. M. Marcus, and M. Scheffler, Phys. Rev. Lett. **78**, 3892 (1997).
- [14] F. Jona and P. M. Marcus, Phys. Rev. B **65**, 155403 (2002).
- [15] P. M. Marcus, F. Jona, and S. L. Qiu, Phys. Rev. B **66**, 064111 (2002).
- [16] E. Wimmer and A. J. Freeman, Fundamental of the electronic structure of surfaces, in *Electronic structure*, edited by K. Horn and M. Scheffler, volume 2, chapter 1, Elsevier, Amsterdam, 2000.

-
- [17] W. Kohn and P. Vashishta, General density functional theory, in *Theory of the inhomogeneous electron gas*, edited by S. Lundqvist and N. H. March, Plenum Press, New York, 1983.
- [18] H. Eschrig, *Optimized LCAO method and the electronic structure of extended systems*, Akademie-Verlag, Berlin, 1989.
- [19] W. Kohn, Rev. Mod. Phys. **71**, 1253 (1998).
- [20] J. P. Perdew and S. Kurth, Density functionals for non-relativistic coulomb systems, in *Density functionals: theory and applications*, edited by D. P. Joubert, volume 500 of *Lecture Notes in Physics*, Springer Verlag, Berlin, 1998.
- [21] J. Kohanoff and N. I. Gidopoulos, Density functional theory: basics, new trends and applications, in *Handbook of molecular physics and quantum chemistry*, edited by S. Wilson, volume 2, John Wiley & Sons, Chichester, 2003.
- [22] M. Levy, Phys. Rev. A **26**, 1200 (1982).
- [23] E. H. Lieb, Int. J. Quantum Chem. XXIV **24**, 243 (1983).
- [24] J. P. Perdew and Y. Wang, Phys. Rev. B **45**, 13244 (1992).
- [25] N. W. Ashcroft and N. D. Mermin, *Solid state physics*, Thomson Learning, 1976.
- [26] E. C. Bain, Trans. AIME **70**, 25 (1924).
- [27] S. L. Qiu, P. M. Marcus, and Hong Ma, Phys. Rev. B **64**, 104431 (2001).
- [28] L. B. Freund and S. Suresh, *Thin film materials: stress, defect formation and surface evolution*, Cambridge University Press, New York, 2003.
- [29] J. Kübler, *Theory of itinerant electron magnetism*, Oxford Science Publication, New York, 2000.
- [30] E. C. Stoner, Proc. R. Soc. A **169**, 339 (1939).
- [31] P. Villars and L. D. Calvert, *Pearson's handbook of crystallographic data for intermetallic phases*, volume 4, ASM international, Materials Park, Ohio, 2nd edition, 1991.
- [32] K. Koepernik and H. Eschrig, Phys. Rev. B **59**, 1743 (1999).
- [33] G. Dahlquist and A. Bjorck, *Numerical methods*, Prentice-Hall Inc., New York, 1974.

-
- [34] W. H. Press, S. A. Teukolsky, W. T. Vetterling, and B. P. Flannery, *Numerical recipes in C – The art of scientific computing*, Cambridge University Press, Cambridge, 2nd edition, 1992.
- [35] A. Möbius, *J. Phys. C* **21**, 2789 (1988).
- [36] X. Z. Ji, Y. Tian, and F. Jona, *Phys. Rev. B* **65**, 155404 (2002).
- [37] P. Blaha, K. Schwarz, and J. Luitz, *WIEN97*, Vienna University of Technology, 1997.
- [38] J. F. Nye, *Physical properties of crystals: their representation by tensors and matrices*, Oxford University Press, London, 1960.

Acknowledgement

To Prof. Dr. H. Eschrig, director at the “Leibniz Institute for Solid State and Materials Research Dresden”, I am grateful for offering me the possibility to write my diploma thesis under his guidance, the pleasant working environment and various support.

I am much obliged to my supervisor Dr. M. Richter, head of the group “Numerical Solid State Physics and Simulation”, for his ongoing encouragement, ideas, suggestions and the patience in discussions.

I would like to thank all members of our working group, especially Dr. K. Koepnik for assistance in calculations with FPLO and Dr. A. Möbius for discussion regarding the error analysis.

Also I want to acknowledge the technical assistance of U. Nitzsche in all computational issues.

Eidesstattliche Erklärung

Ich versichere, dass ich die vorliegende Diplomarbeit selbständig verfasst und keine anderen als die angegebenen Quellen und Hilfsmittel benutzt habe; aus fremden Quellen übernommene Passagen und Gedanken sind als solche kenntlich gemacht. Diese Arbeit hat in gleicher oder ähnlicher Form noch keiner Prüfungsbehörde vorgelegen.

Stephan Schönecker